REPORT DOCUMENTATION PAGE

AFRL-SR-AR-TR-04-

05605

1. AGENCY USE ONLY *(Leave blank)*	2. REPORT DATE	3. REPORT TYPE AND DATES COVERED
	2 NOV 04	FINAL REPORT 15 JUN 03 - 14 FEB 04

4. TITLE AND SUBTITLE
NANOGAP BIOMOLECULAR JUNCTION

5. FUNDING NUMBERS

F49620-03-1-0367

6. AUTHOR(S)
DR LUKE P. LEE

7. PERFORMING ORGANIZATION NAME(S) AND ADDRESS(ES)
UNIVERSITY OF CALIFORNIA, BERKELEY
DEPARTMENT OF BIOENGINEERING
455 EVANS
BERKELEY, CA 94720-1740

8. PERFORMING ORGANIZATION REPORT NUMBER

9. SPONSORING/MONITORING AGENCY NAME(S) AND ADDRESS(ES)

AFOSR/NL
4015 WILSON BLVD., ROOM 713
ARLINGTON, VA 22203-1954

10. SPONSORING/MONITORING AGENCY REPORT NUMBER

11. SUPPLEMENTARY NOTES

12a. DISTRIBUTION AVAILABILITY STATEMENT

APPROVE FOR PUBLIC RELEASE: DISTRIBUTION UNLIMITED

12b. DISTRIBUTION CODE

13. ABSTRACT *(Maximum 200 words)*

The overall goal of this work is to develop the capability to create platforms with a small array that will be able to sense and identify a wide range of chemicals using real-time measurements to determine both the dynamics of biomolecular reactions as well as quantitative differences in binding characteristics. The specific goals of this project are to develop and understand the physiochemical mechanisms of a nanogap dielectric biosensor that has recently been demonstrated at BSAC. These devices, which are fabricated using standard CMOS technology, have the potential to serve as biomolecular junctions because their size reduces electrode polarization effects regardless of frequency. This junction technology is essentially a 'biology-to-digital' converter system that enables real time conversion of biomolecular dielectric signals into digital information. Preliminary work using nanogap sensors to sense biomolecular binding has demonstrated a four order of magnitude increase in sensitivity over existing fluorescence techniques. Bacause sensors based on nanoscale gaps have not existed before, in order to exploit their capabilities in a sensor array, it will be critical to increase our understanding of their perfor-mance and to develop the tools required to integrate them into a sensor platform. Toward this goal, a series of experimental and modeling tasks are proposed that will investigate the physiochemical characteristics of the nanogap junctions. During this process, the nanogap junctions will also provide insight into fundamental biomolecular physics and processes applicable to other DARPA/DSO programs.

14. SUBJECT TERMS

20041112 033

15. NUMBER OF PAGES

16. PRICE CODE

17. SECURITY CLASSIFICATION OF REPORT	18. SECURITY CLASSIFICATION OF THIS PAGE	19. SECURITY CLASSIFICATION OF ABSTRACT	20. LIMITATION OF ABSTRACT

BEST AVAILABLE COPY

Final Report

Nanogap Biomolecular Junction

Principal Investigator: Luke P. Lee

Co-PI: Dorian Liepmann

Department of Bioengineering
University of California, Berkeley

Administrative Point of Contact:
Ms. Patricia Gates
Senior Research Administrator
Sponsored Projects Office, 336 Sproul Hall
University of California at Berkeley
Berkeley, CA 94720-5940
(510) 642-8109, (510) 642-8236 (Fax)
pgates@uclink4.berkeley.edu

1. RESEARCH OBJECTIVES

The overall goal of this work is to develop the capability to create platforms with a small array that will be able to sense and identify a wide range of chemicals using real-time measurements to determine both the dynamics of biomolecular reactions as well as quantitative differences in binding characteristics. The specific goals of this project are to develop and understand the physiochemical mechanisms of a nanogap dielectric biosensor that has recently been demonstrated at BSAC. These devices, which are fabricated using standard CMOS technology, have the potential to serve as biomolecular junctions because their size reduces electrode polarization effects regardless of frequency. This junction technology is essentially a 'biology-to-digital' converter system that enables real time conversion of biomolecular dielectric signals into digital information. Preliminary work using nanogap sensors to sense biomolecular binding has demonstrated a four order of magnitude increase in sensitivity over existing fluorescence techniques.

Because sensors based on nanoscale gaps have not existed before, in order to exploit their capabilities in a sensor array, it will be critical to increase our understanding of their performance and to develop the tools required to integrate them into a sensor platform. Toward this goal, a series of experimental and modeling tasks are proposed that will investigate the physiochemical characteristics of the nanogap junctions. During this process, the nanogap junctions will also provide insight into fundamental biomolecular physics and processes applicable to other DARPA/DSO programs.

2. MAJOR ACOMPLISHMENTS

- Nanogap sensor characterizations of non-electrolyte & electrolyte
- DNA detection in 1x phosphate-buffered saline (1x PBS) – effect of electrode polarization, *in situ* hybridization
- Ultra-fast electric pulse-assisted DNA immobilization and hybridization
- Protein-small molecule (Streptavidin-biotin) interaction study
- Solid-phase immunoassay (Laminin)
- Modeling of solid phase DNA hybridization kinetics, i.e. dsDNA concentration as a function of time
- Calculations of hybridization time as a function of various parameters, such as effective target ssDNA concentration, probe ssDNA density, and hybridization binding rate
- Modeling electrical field-assisted target ssDNA transport for achieving fast immobilization and hybridization
- Study of double layer capacitance changes as a function of surface density (molecular packing)
- Development of electrical circuit model for nanogap response
- <u>First demonstration of protein folding/unfolding detection by nanogap-based low frequency dielectric relaxation spectroscopy.</u>
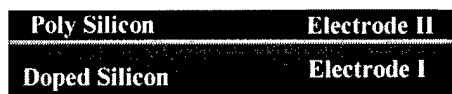
3. Background

<u>Experimental Protocol</u>

The silicon-based horizontal nanogap device was employed for most experiments since the last report because it could be fabricated with the highest yields. This design features an oxide spacer 20-100 nanometers thick between electrodes of poly-Si and a highly doped Si substrate. The fabrication sequence and SEM pictures of a finished device are included below.

PSG

Silicon wafer

1. Deposit 1 μm PSG by LPCVD

Doped Silicon

2. Diffusion and Remove the PSG in HF

| Poly Silicon | Electrode II |
| Doped Silicon | Electrode I |

3. Thermal oxidation and deposit Poly-Si

| Poly Silicon | Electrode II |
| Doped Silicon | Electrode I |

4. Dry etching of Poly-Si and wet etching of Oxide; Box area shows the fabricated nanogap electrodes
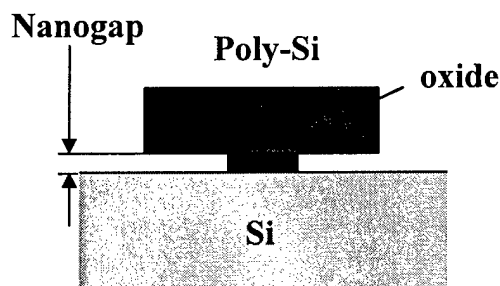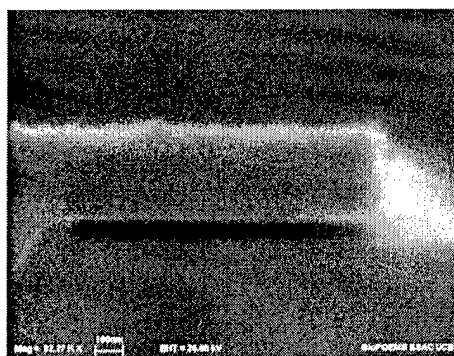
Nanogap   Poly-Si   oxide

Si

Figure 1: Process flow, micrographs, and schematic of Si horizontal nanogap device.

Experiments were performed sweeping frequencies from 1 Hz to 1 MHz using a Novocontrol Alpha-N dielectric analyzer with 30 mV input signal (0 V D.C. offset) to minimize heating effects of the biological sample, in referencing mode. Using this mode, in which impedance measurements are compared against internal components, allows the highest accuracy available. Full calibrations to the reference plane of wafer probe station coaxial cables were performed monthly and/or anytime the analyzer was moved.

To load a liquid sample, 20-30 μL was pipetted into the nanogap by placing a small silicone rubber slab with a 2-3 mm circular opening on top of the device as shown:
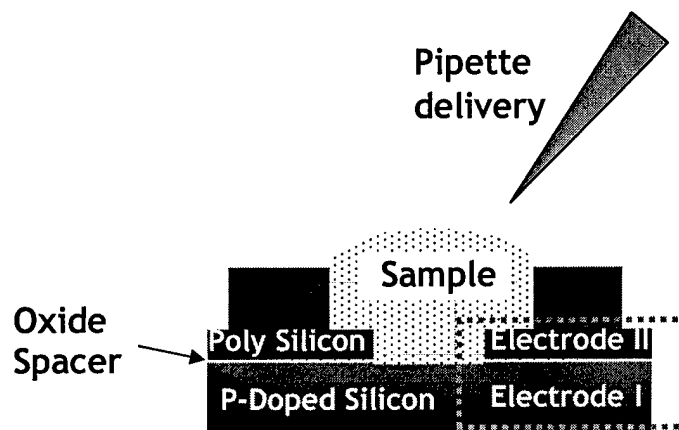
3

Figure 2: Schematic showing loading of device by dispensing from pipetter.

A 2-point probe measurement using Signatone S-series micropositioners was done with the chips held by vacuum to the chuck. Data taken with suspect contacts were duplicated or triplicated where necessary.

Lumped Element Models

By measuring the serial impedance, we found a simple electrical model of a resistor (representing the substrate and poly-Si) and capacitor in series describes the behavior of the device with no liquid:
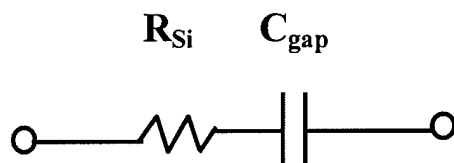

Figure 3: Lumped-element model of dry nanogap electrodes.

Because of the oxide spacer, the nanogap capacitance above is really two capacitors in parallel: the oxide portion and the part actually defining the gap, which we'll call "sample" (see Fig. 2):
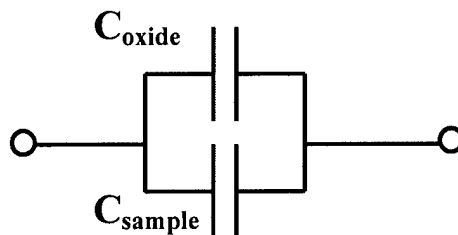

Figure 4: Lumped-element model of spacer and gap

4

If we combine this into one model, we find the capacitance of a typical 22 nm gap size sensor is roughly 300 pF and the resistance of the poly-Si and silicon substrate contacts is about 2.3 kΩ:
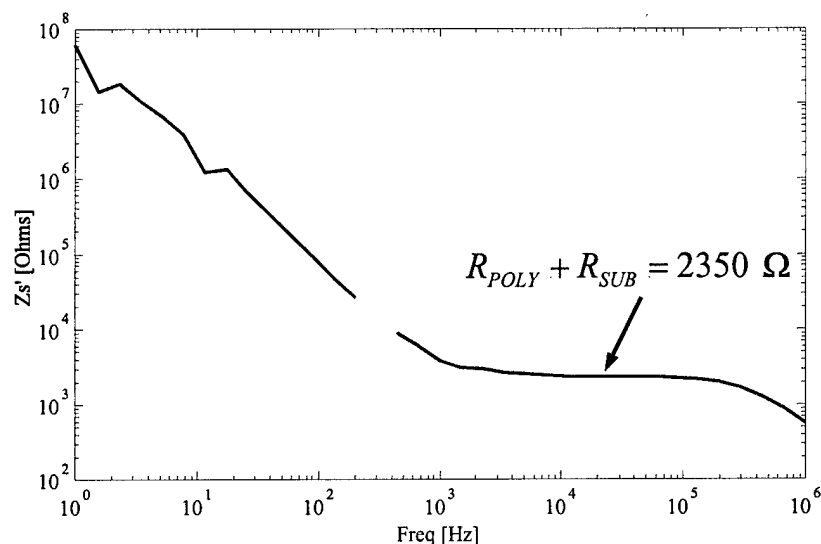
$$R_{POLY} + R_{SUB} = 2350 \ \Omega$$

Figure 5: Measurement of serial impedance of a nanogap (dry), showing resistance of substrate/poly-Si. At sufficiently high frequencies, C_{gap} is shorted out and this value can be extracted.

Zs''=15 Ω at 1MHz
(L=2.4μH)
negligible compared to
poly and substrate
lead resistance
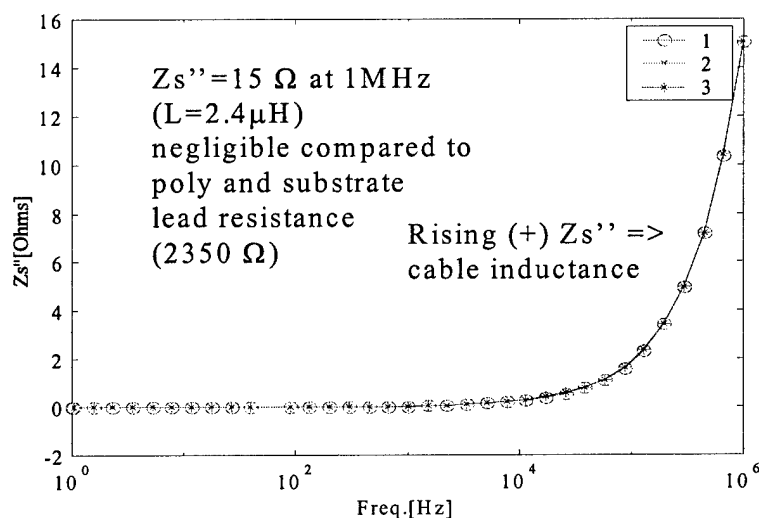(2350 Ω)

Rising (+) Zs'' =>
cable inductance

Figure 6: Measurement of serial impedance of a nanogap (dry) with tips touching (shorted), showing cable inductance is small beside device resistance for three trials.
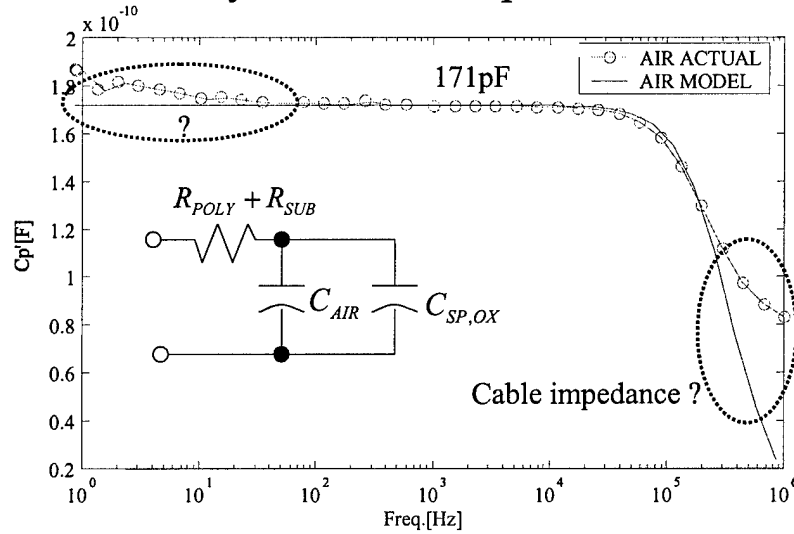
5

Dry Measured Capacitance

Figure 7: Simple electrical model of dry nanogap device. Model is accurate for 100 Hz ~ 100 kHz but deviates at very low and high frequencies. Both these effects were noted also in testing a 33 pF ceramic capacitor, suggesting a system rather than device response. The increase at the lowest frequencies is most likely due to additional stray elements from poor isolation of the device and probe tips. From Fig. 5, it appears there is a very small stray capacitance causing a high frequency roll-off, which may be due to stray capacitances in the cable (part of it was only braid shielded, but not thicker coaxial cable).

Because the nanogap is designed as a capacitor, we generally program the analyzer to measure capacitance and loss tangent (ratio of capacitive reactance to resistance). Below is a typical measurement for a device with 22 nm gap size, showing a capacitance near 300 pF and loss tangent $< 10^{-1}$ below 10 kHz:
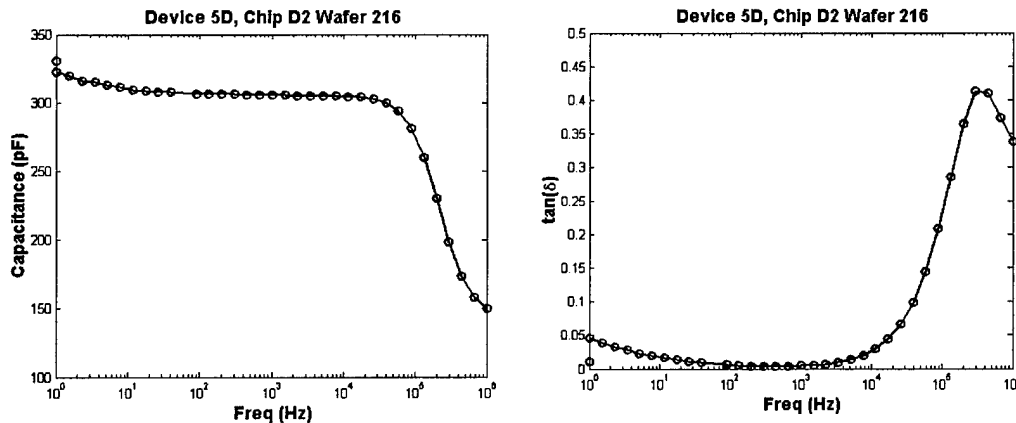

Figure 8: Capacitance and loss tangent measurements of a device in air.

Above 100 MHz, the reactive term is small and the impedance is controlled by the electrode resistance. In addition, our probe station measurements were limited to 3 MHz because of the inductance of the cables and the BNC connectors.

Effective Permittivity Calculation

In order to convert the capacitance and loss measurements into permittivity, we make some assumptions about the device, namely that we can ignore the fringing E-field at the edge of the device, treat it as two 'parallel plates', and the sample itself (liquid) dominates the impedance. Because this may not necessarily be the case, we term the dielectric parameters "effective" permittivity.

The relationship between the total capacitance and the permittivity for the oxide and sample in parallel can be written is as follows:

$$C = \frac{\varepsilon_0}{d}\left(\varepsilon_{ox}A_{ox} + \varepsilon_{sample}A_{sample}\right) \quad (1)$$

where C is the total measured capacitance, ε_0 is the permittivity of vacuum, d is the nanogap spacing, and 'ox' (oxide) and sample parameters are the relative permittivity and areas of the electrodes, respectively. If the sample is air, then $\varepsilon_{sample} \sim 1$, and we can rearrange and compute the relative permittivity of oxide:

$$\varepsilon_{ox} = \frac{1}{A_{ox}}\left(\frac{Cd}{\varepsilon_0} - \varepsilon_{sample}A_{sample}\right) \quad (2)$$

If the area of the oxide spacer is ~195,000 μm^2, the sample ~71,000 μm^2, measured capacitance is 305 pF, gap spacing 21.6 nm, then the oxide relative permittivity is about 3.5. This is a bit lower than the 3.8 ~ 5.5 reported for thermally grown, thin films, but close.

Once we know the oxide permittivity, we can rearrange to compute the permittivity from the measured capacitance and device geometry of the sample:

$$\varepsilon_{sample} = \frac{1}{A_{sample}}\left(\frac{Cd}{\varepsilon_0} - \varepsilon_{ox}A_{ox}\right) \quad (3)$$

This allows us to compute the real permittivity of the sample, ε_{sample}', often referred to as the dielectric constant (for low frequencies). To obtain the imaginary part (ε_{sample}''), we multiply the loss tangent by this factor since:

$$\tan(\delta) = \frac{\varepsilon''}{\varepsilon'} \quad (4)$$

The idea behind using nanogap junction electrodes is that we can employ a simple, 2-probe electrode measurement for studying biomolecular interactions using a common electrode material (silicon/poly-Si). In making dielectric measurements in conducting liquids at low frequencies, it is essential to compensation for electrode polarization, a phenomenon that impedes direct measurement of the liquid due to charges accumulating at the electrode surfaces. We'll briefly revisit the theory of the electrical double layers, reviewing the strategy to exploit the overlapping double layers in the nanogap device to measure dielectric properties of the sample.

Electric Double Layer – Electrochemical Description

The behavior of an electrode/electrolyte interface is much like a capacitor. Since good conductors do not support electric fields internally at equilibrium, all charge in the electrode resides on the surface. The earliest description by Helmholtz [14] postulated two layers of opposite charges right at this junction (hence the name "double layer"). Specifically adsorbed species and solvent molecules for the inner layer, often called the Stern (or Helmholtz or compact) layer. This theory was later modified by Guoy, Chapman, and later Stern (to account for high ionic concentrations – very thin, compact layers) by allowing nonspecifically absorbed ionic species (solvated ions) in solution to extend in a so-called diffuse layer away from the electrode surface. This view takes into account thermal forces that also influence the equilibrium distribution of counterions in solution. The total excess charge density in solution is thus the sum of the charge in the Stern and diffuse layers.
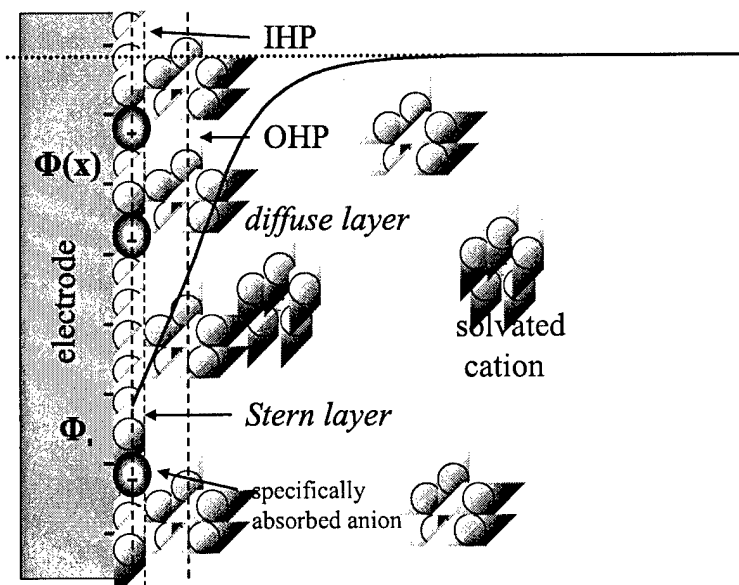

Figure 9: Illustration of double layer capacitance using Guoy-Chapman model. Diffuse layer thickness, and hence double layer, has been shown experimentally to be a function of applied potential and ionic concentration.

Assuming the surface charge is continuous and uniform and the ions in solution are point charges, the Poisson equation for the double layer may be solved for a small surface potential (25 mV at ambient temperature) by making the Debye-Hückel approximation [1]. This allows us to write the double layer thickness as:

8

$$\frac{1}{\kappa} = \sqrt{\frac{\varepsilon \, kT}{2n_0 z^2 e^2}} \quad (5)$$

where ε is permittivity, k is Boltzmann's constant, z the valence of the species, T the absolute temperature, e charge of an electron, and n_0 the concentration of the species. For a 1 mM NaCl solution, this distance is about 9.6 nm. The nanogap electrodes can be fabricated with gap spacing in the range of 15 to 300 nm, allowing the electrical double layer at each electrode to overlap each other at sufficiently low ionic strength.

We can define a unit less parameter $S_n = \kappa L$, where L is the distance between nanogap electrodes. When this parameter is of order unity or smaller, the potential distribution become more uniform across the entire gap and we are particularly sensitive to changes in the double layer capacitance.
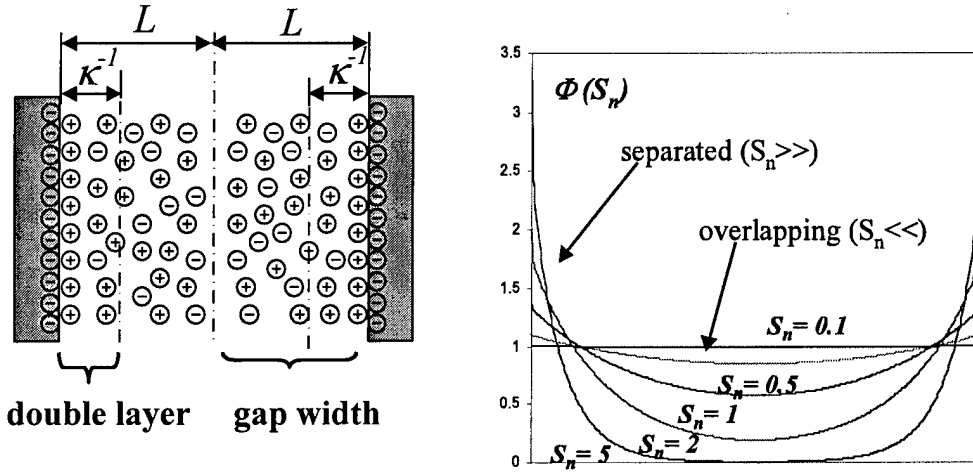

Figure 10: Illustration of double layer capacitance and electrode spacing for nanogap device.

If the gap size is much larger than the electric double layer (or we use a high enough ionic strength solution, so the double layers do not overlap), the polarization impedance, as described previously, is exceedingly large. Under these conditions, it is difficult to discern any changes in the solution caused by dielectric relaxation of the species present since the device is not sensitive to small changes in the polarization impedance (see Section C under "Major Accomplishments").

If, however, the ionic strength and size of the nanogap are judiciously chosen to obtain overlapping double layers and we suitably immobilize species of interest, we should be able to move the location of the inner charge (Stern) layer toward the center of the gap. If coverage of the electrode is sufficiently dense, this should block the surface from allowing in-phase current flow, adding another capacitance in series. In effect, we modulate the double layer thickness by specifically attaching these biomolecules. If the

9

density is not high enough though, charge leakage through this layer will not greatly modify the double layer, leading to loss of sensitivity.
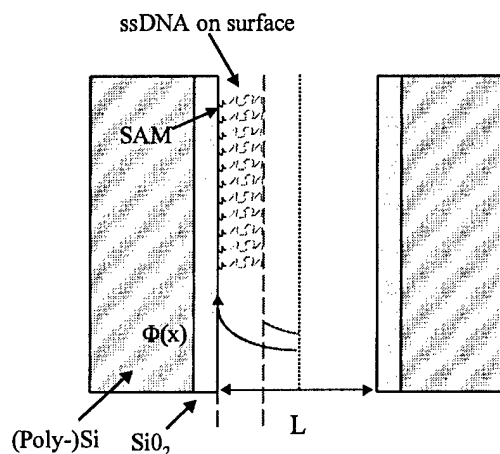

Figure 11: Illustration of changing the double layer capacitance using an amine-terminated self-assembled monolayer (SAM) to attach single stranded DNA to the surface. If this layer is suitably packed and thus blocking, the location of the inner Helmholtz plane (and the double layer) should change from blue to green.

For discussion of solution phase detection of DNA in the nanogap and comparison to dielectric relaxation theory of polyelectrolyte, please see attached paper at end of report.

Electric Double Layer – Lumped Element Model

Because of the presence of ions within a few nanometers of the electrode surface, an electric double layer forms that strongly influences the measured impedance. This effect is typically modeled as a resistor and capacitor in series with the liquid sample, R_p, C_p, which is in turn represented as an RC parallel circuit (the combination of mobile charges and dielectric loss being the resistive element):
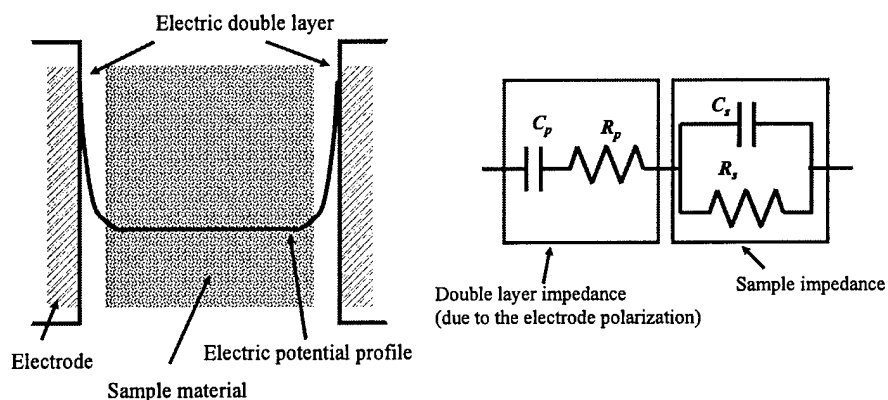

Figure 12: Diagram of electric potential as a function of distance from electrode surface and serial electrical model typical of electrodes with gap sizes above 100 nm.

If we write expressions for the aggregate, measured capacitance and resistance for this case, we obtain:

$$C_m = C_s + \frac{1}{\omega^2 R_m{}^2 C_p} \quad (6)$$

$$R_m = R_s + R_p + \omega^2 R_m{}^2 C_m{}^2 R_s \quad (7)$$

It is evident that at low frequencies the second addend in the capacitive term will increase enough to dominate the measured capacitance (as the square of the frequency), while the resistance will approach the sum of the sample and polarization resistances.

We previously proposed that the double layer impedance might be considered in parallel with the double layer capacitance:
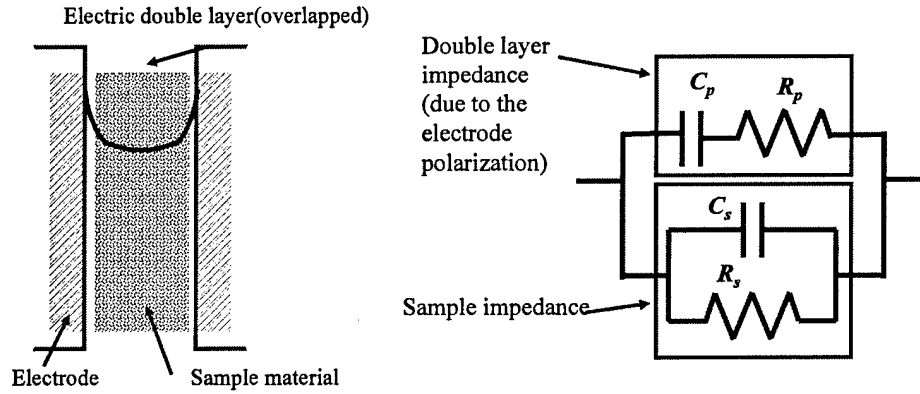

Figure 13: Diagram of electric potential as a function of distance from electrode surface and parallel electrical model originally proposed to represent nanogap electrodes.

This seemed reasonable, as the electric potential distribution across the gap is more uniform. If this is the case, however, then the smaller impedance (in contrast to the serial model) should more strongly affect the overall measured impedance. In order to measure the intrinsic sample, this means the sample impedance should be small beside the electrode polarization impedance. For this model:

$$C_m = \frac{C_p}{1 + \omega^2 C_p^2 R_p^2} + C_s \quad (8)$$

$$\frac{1}{R_m} = \frac{\omega^2 C_p^2 R_p}{1 + \omega^2 C_p^2 R_p^2} + \frac{1}{R_s} \quad (9)$$

Thus, $C_m \sim C_p + C_s$ and $R_m \sim R_s$ at low frequencies, so there is no second order increase of the polarization capacitance and the measured resistance is nearly intrinsic to the sample.

11

However, from our further investigation, it appears there is inverse power law dependence across all frequencies. This suggests we are in fact sensitive to the polarization elements and the parallel model is not a good description. By overlapping the double layers, we have perhaps reduced the sample impedance to the point where the polarization impedance dominates the measurement. Since the double layers overlap and the potential are nearly constant across the whole gap, the sample impedance is of little consequence. This is best demonstrated by the data for various concentrations for an electrolyte (NaCl), which changes the double layer capacitance and a non-electrolyte (glucose), which simply reduces the effective permittivity slightly due to the presence of solvated sugar molecules in the gap (Sections A under "Major Accomplishments").

Below is a typical dielectric spectrum for deionized water, showing three apparent dispersions between 1 Hz and 1 MHz. The peak at ~100 Hz is due to the presence of a thin surface oxide on the device and was confirmed this summer using an electrochemical approach. The peak in the 1-10 kHz range is due to the electric double layer and changes with the ionic strength (see Fig. 1 – NaCl solutions at different concentrations). The last peak in the 100 kHz region is related to probe tip contact.
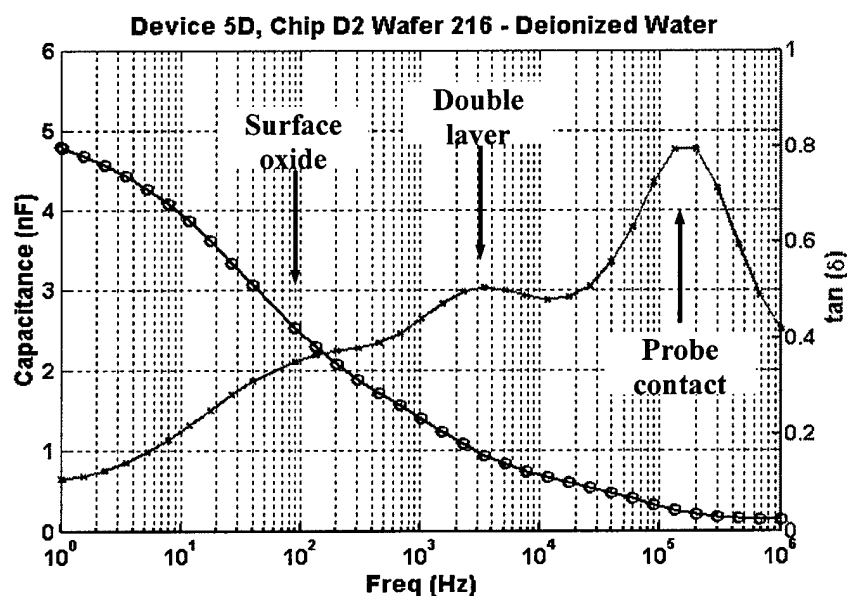

Figure 14: Capacitance and loss tangent measurements of a device in deionized water. Note the presence of three apparent dispersion peaks and the inverse power dependence of the capacitance with frequency for the whole range.

12

A. Electrolyte Permittivity for Various Concentrations, Gap Sizes

Various concentrations of sodium chloride (NaCl) in deionized water were introduced into the nanogap, beginning with the smallest concentration first and proceeding to the largest. In between, the sample was removed by capillary wicking using a clean, absorbent slip of cloth. As can been seen for the 22 nm example, the signal of deionized water can be recovered by rinsing 3 times in DI and measuring the fourth 30 μl aliquot.
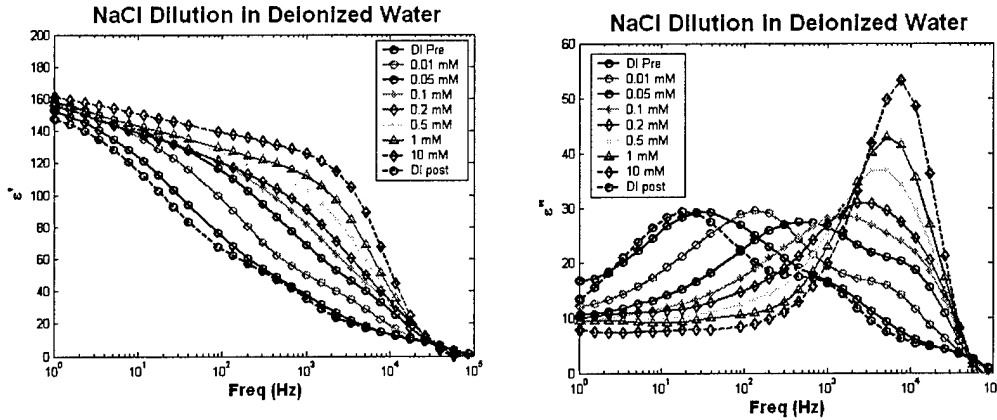

Figure 15: Effective permittivity of various concentrations of sodium chloride in deionized water in 22 nm gap.

We note the greatest changes are in the frequency range between 10 and 10,000 Hz (10 kHz). Lower than 10 Hz the response is dominated by the charge accumulation at the electrodes, even for deionized water, and larger than 10 kHz the capacitance of the oxide between the poly-silicon and silicon electrodes is shorted out. We can see the general effect of changing the double layer is to increase the real permittivity (especially at lower frequencies) while increasing the slope at higher frequencies (similar to the analogy of a single RC circuit roll-off). The loss peak is also shifted higher in frequency, and the small peak around 100-200 Hz, which has been shown, using electrochemical methods to be a thin, native oxide covering the silicon, is no longer visible.

For each gap size, we measured a range of NaCl concentrations so that we adequately covered the point when the double layer thickness, defined as the reciprocal of the Debye-Hückel parameter (κ) :

$$\kappa = 3.288 \sqrt{I} \quad \text{at 298 K} \quad (10)$$

was equal to the gap size. Here I is the ionic strength in molarity and $1/\kappa$ is the double layer thickness in nm. For 22, 44, and 97 nm gaps, the concentrations at which twice the double layer thickness equals the gap size are 0.764, 0.191, and 0.0385 mM NaCl respectively. Again, for the 22 nm gap, the most relevant frequencies to observe this change are in the mid-band, maximized between 100 Hz and 5 KHz. Since ε' increases in an easily observed fashion, we plot each gap size in a different color, normalizing each experiment to the permittivity of deionized water. The dotted lines represent where the gap is approximately twice the thickness of the double layer for easy identification.
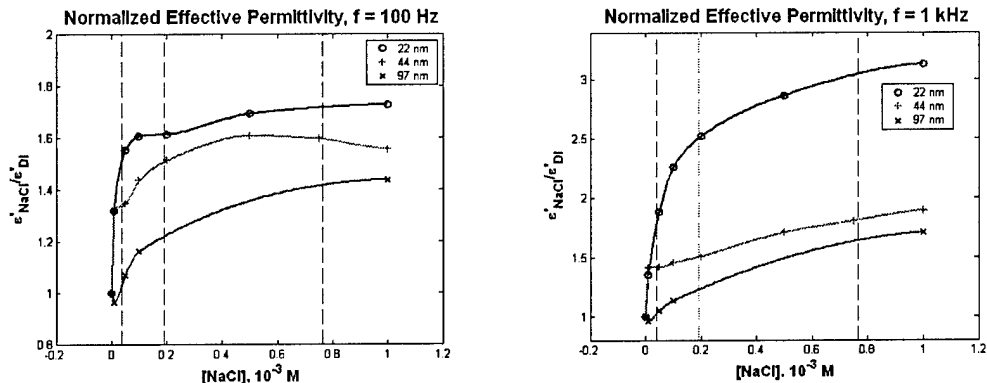
13

Figure 16: Permittivity of three nanogap sizes relative to deionized water for various concentrations of sodium chloride at two frequencies. Dashed vertical lines denote point when gap size is twice double layer width.

At concentrations above the dashed line for a given nanogap size, the electrical response only slowly varies, since very small changes in the double layer capacitance are difficult to resolve when the thickness becomes ~ few nm. This should correspond to a saturation effect in which the ratio between the permittivity of the salt solution and water is roughly constant. This is observed particularly well for the two smaller gaps at 100 Hz. If we return to Fig. 1 and follow the lines upward across increasing concentrations, we can see the space between them shrinks at the highest concentrations. This implies our measurement will be dominated by double layer capacitance at typical buffer concentrations for physiological work (> 1 mM, typically 10-150 mM). However, it means we can take advantage of changing this same double layer capacitance by immobilizing molecules on the surface of our devices that, in effect, change the gap spacing.

B. Nanogap Characterization using Non-electrolyte

In order to understand the device response to small, non-ionic substances in solution, a non-electrolyte was chosen avoid changing the double layer capacitance. Reagent-grade glucose was diluted in deionized water and measured in a 22 nm gap chip.
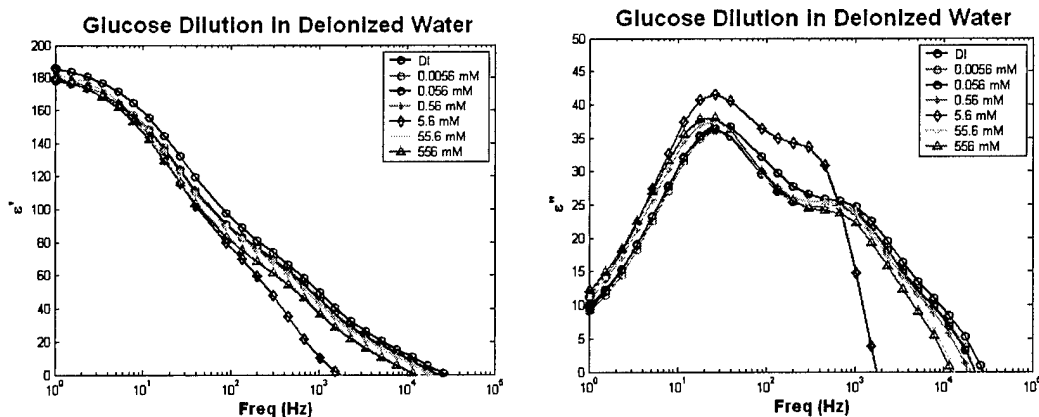
14

Figure 17: Effective permittivity of various concentrations of glucose in deionized water in 22 nm gap.

As can be seen, there is a decrease in permittivity with increasing concentration of glucose in the gap. This is consistent with mixture theory, since water molecules are replaced with hydrated glucose in the active part of the device. Previous studies have confirmed this trend [3]. We note also the shapes of the curves are preserved in frequency, demonstrating the large increase noted before for NaCl is indeed an ionic effect. The data point at 5.6 mM is an anomaly most likely caused by disturbing the chip when exchanging liquids. If this point is rejected, we can examine the trend at one frequency by taking a slice of the above plot:
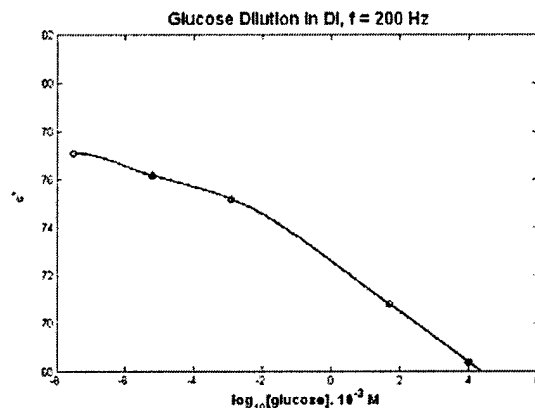

Figure 18: Effective permittivity of various concentrations of glucose at a single frequency.

The change across six logs of concentration is only about 10-15% at 200 Hz and is similar at other frequencies (Fig. 17).

C. DNA in 1x Phosphate-buffered Saline (1x PBS) – Effect of Electrode Polarization, *In Situ* Hybridization

In order to test the dielectric properties of single and double stranded DNA (ss/dsDNA), we hybridized 20-mer oligonucleotides in 1x PBS solution at 42 °C for three hours and compared the response to ssDNA alone (by combining two mismatched 20-mer

15

sequences). Both DNA samples were in the same buffer, which was also measured by itself to serve as a blank. Using nanogap electrodes with high ionic strength solutions, however, is extremely difficult, since the salt masks changes in dispersion from molecular structure. Below, we show the permittivity of ssDNA (S1-S3), dsDNA (8 mM conc., if 100% hybridized – S1-S2), and 1x PBS in the nanogap:
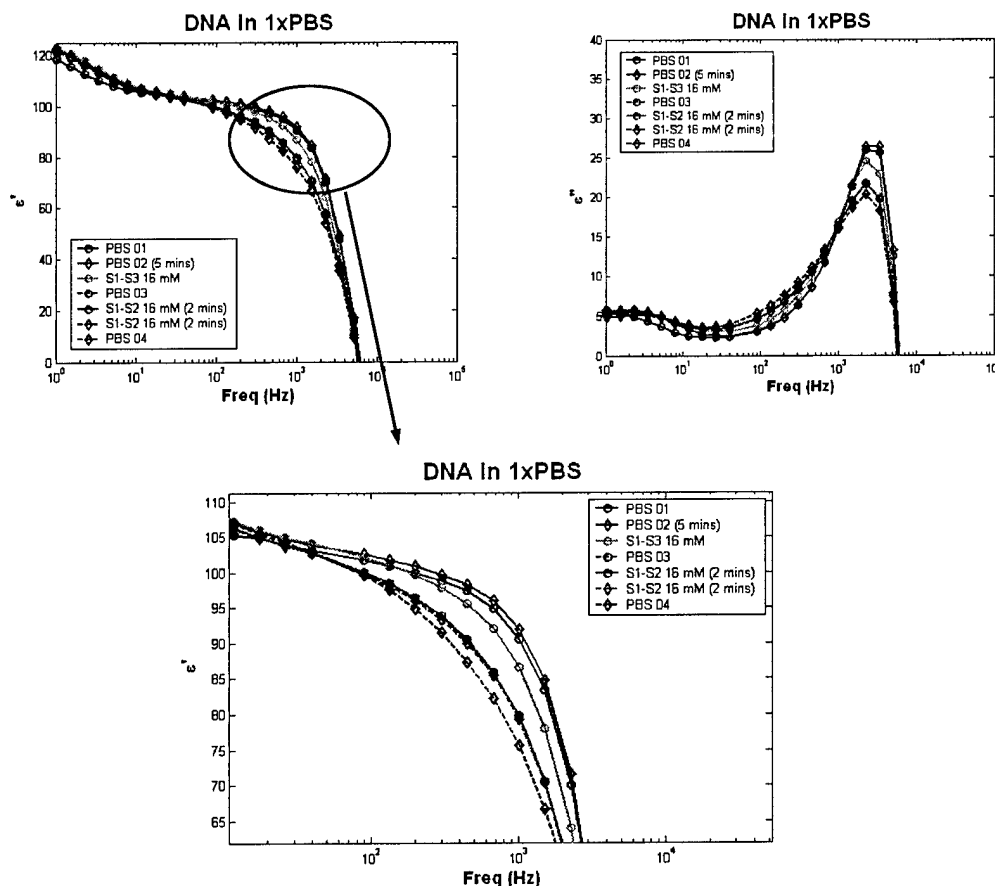

Figure 19 (a),(b),(c): Effective permittivity of ssDNA (S1-S3), dsDNA (S1-S2), and 1xPBS buffer. PBS run number corresponds to time of measurement. Drift is probably due to small temperature variations during the course of the measurement. Parenthetic time denotes number of minutes waited before starting measurement.

As is seen from Fig. 19(c), a magnified view of the real permittivity, identifying the presence of macromolecular DNA from background ions is not possible.

D. Single-stranded (ss)DNA in Deionized Water

Because the measurement is sensitive to ionic strength above 1 mM at typical gap sizes, we continued further work using a protocol to immobilize the DNA on the polysilicon & silicon electrode surfaces using a self-assembled monolayer. It is worth revisiting the experiment performed in the last quarter with single stranded DNA in deionized water. Recall our measurements have high ionic sensitivity. The synthesized 20-mers are

16

desalted and lyophilized but still contain residual amounts of salt ions. From the manufacturer, we estimated for in deionized water that concentration of monovalent cations was approximately the number of bases of our DNA strand multiplied by the concentration of DNA utilized. Thus, for ~16 μM DNA (0.1 mg/ml), the concentration of salt is about 0.3 mM:
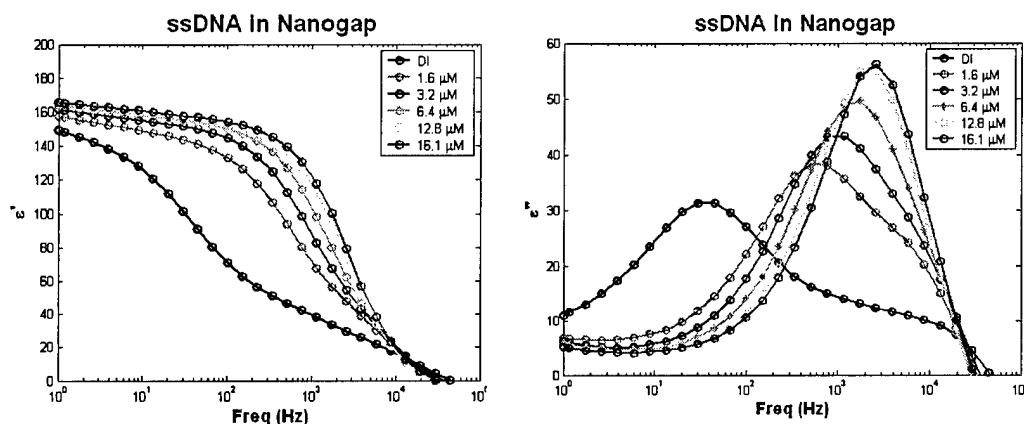

Figure 20: Effective permittivity of ssDNA 20-mer in deionized water at various concentrations. Note similarities to Fig. 1 due to presence of salt in DNA oligonucleotide, although pure NaCl decreases more sharply in the mid-frequencies.

E. Confirmation of Attachment Chemistry Using Glass Coverslips

In order to measure DNA in a low salinity solution, we functionalized silicon dioxide using a silanizing compound, 3-aminopropyltriethoxysilane, to create amine groups on the native SiO_2 surface that forms spontaneously on the silicon chips. We could then attach the DNA oligos that are phosphorylated on the 5'-end via a phosphoramidate linkage using a non-phosphate containing buffer (0.1 M N-methylimidazole). This allows us to attach the DNA using an imidazole buffer, hybridize in phosphate-buffered saline (PBS), and carryout dielectric spectroscopy in deionized water to avoid ionic effects.

We validated the attachment chemistry using glass cover slips functionalized with the SAM at several concentrations. The DNA was fluorescently labeled with a rhodamine dye (TAMRA) at the 3'-end. As controls, we used a non-phosphorylated DNA strand with a different fluorescent tag (fluorescein) and a glass slide with no SAM.
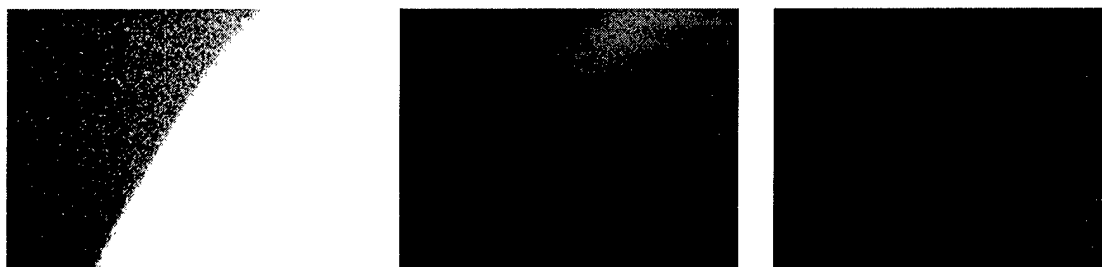
17

Figure 21: 3'-TAMRA modified ssDNA immobilized on surface of glass coverslip at 16, 1.6, and 0.16 μM concentration. No fluorescence above background was observed using non-phosphorylated DNA nor non-specifically bound DNA on an unfunctionalized cover slip.

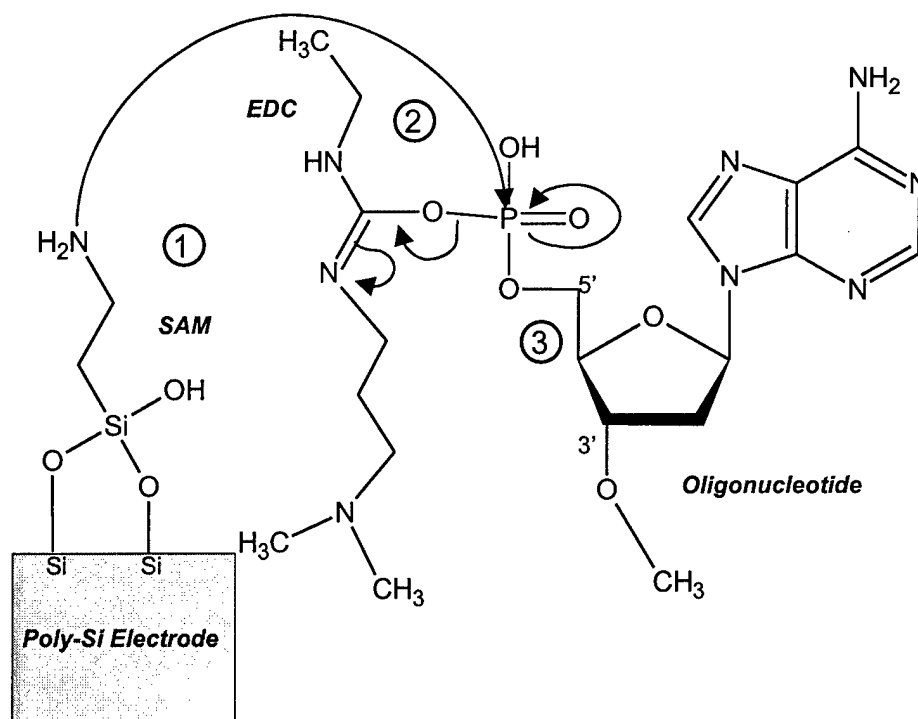The details of the immobilization chemistry are below:

Figure 22: 1) native oxide on the poly-Si electrodes silanized with an amine-terminated oxysilane 2) intermediate binding of (1-ethyl-3-(3-dimethylaminopropyl) carbodiimide hydrochloride (EDC) to 5'-phosphate modified DNA 3) completion of linkage by phosphoramidate bond to attach DNA to SAM.

F. Measurement of surface-bound DNA Immobilization and Hybridization After Rinsing in Deionized Water

Because of the problems detailed in the previous sections, we devised two strategies to measure in deionized water (ionic strength $\sim 10^{-7}$ M). Firstly, we carried out DNA immobilization and hybridization protocols in higher ionic strength buffers (100 mM imidazole and 150 mM saline, respectively) and subsequently washed the devices in

deionized water (DI), measuring the dielectric properties after rinsing. Alternately, we simply diluted the buffers in DI so that the ionic strength was low enough to allow the double layers to overlap.

There are some changes from measurement to measurement that most likely are reflective of the amount of liquid filling the nanogap when samples are exchanged. By measuring permittivity of deionized water as a function of the amount of the sensor exposed to deionized water, we were able to estimate the change in signal per unit length of coverage. This is approximately 0.36 nF/mm and means a 6% change (a typical change at 100 Hz for our controls) corresponds to a variance in sensor coverage of about 300 um. Differences in filling were confirmed by fluorescence microscopy using tagged DNA at 15 uM concentration.
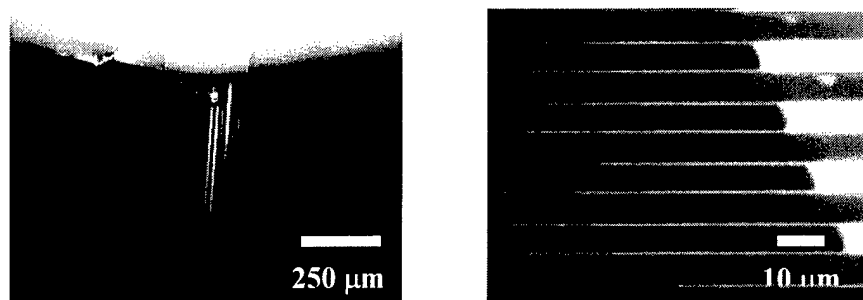

Figure 23: (left) 3'-TAMRA modified ssDNA at 15 μM concentration in silicone well (bright spot at top) filling channels. It was observed channels did not always consistently fill (right), but sometimes stopped at the interfaces of silicone structures used to cover the device.

Building up molecular layers on the surface of the nanogap should change the amount the electrical double layers overlap, if the coverage of these molecules is sufficiently dense to consider the layers "blocking", i.e. that most free charge resides at the end away from the electrode surface. Using this argument, the measured capacitance should decrease (as the double layers overlap more and negate the effect of charge accumulation, since the gap is smaller). This also means a shift of the dispersion to the lower frequencies and is analogous to the effect observed by decreasing salt concentration (see Figs. 15 and 16).
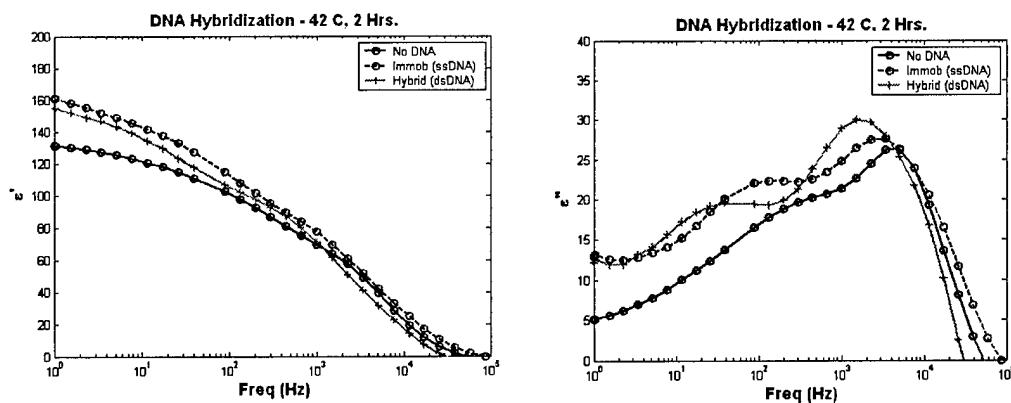

Figure 24: 15 μM DNA immobilized and hybridized on the nanogap, measured in deionized water. Changes in the dielectric properties are caused by attachment of DNA to the surface. The DNA was immobilized in 0.1 M imidazole buffer and hybridized in 1x PBS each at 42 ℃ for 2 hours.

19

We note a significant change in the dispersion peaks after attaching single and double stranded DNA. In both cases, the local loss (ε") maxima are shifted to lower frequencies due to the molecular layers increasing capacitance. The real permittivity appears to have increased as well, which is somewhat unexpected if the double layer overlap increased by building monolayer on the surface.

G. Pulse-assisted DNA Immobilization and Hybridization

Recently, a method for enhancing covalent immobilization and hybridization of DNA on a surface using a DC electric pulse has been presented [19, 20]. Using this methodology, we applied a pulse train with the following parameters to the nanogap at the immobilization and hybridization steps:
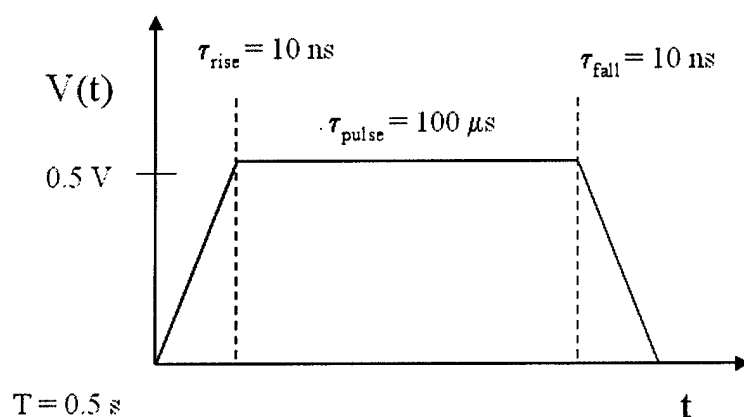

Figure 25: Pulse waveform used for fast immobilization and hybridization.

We applied the signal for about 10 seconds, in which time 20 pulses reached passed through the electrodes. Changes similar to the passive (no pulse) in permittivity were observed:
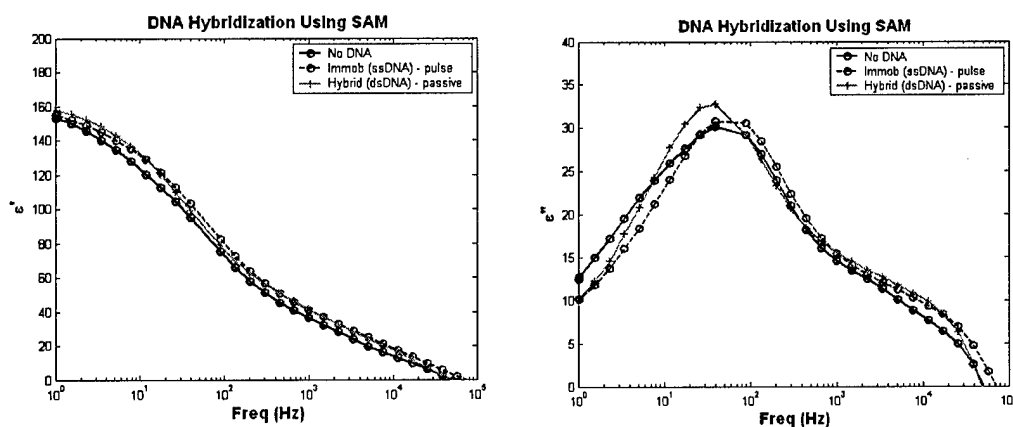

20

Figure 26: 15 □M DNA immobilized and hybridized on the nanogap, measured in deionized water. The DNA was immobilized in 0.1 M N-methyl imidazole buffer and hybridized in 1x PBS each at room temperature for approximately 2 minutes using an electric field pulse-enhanced method.

To further investigate electric pulse assisted immobilization, we followed a protocol similar to the paper mentioned previously [19] to immobilize 3'-TAMRA modified DNA on glass chips with gold electrodes. A pulse train with a period of 10 s was applied for 30 s (roughly three pulses) to initiate the immobilization. All fluorescence images were acquired using a Princeton Instruments CCD camera with 10 ms exposure time. Three SAM-coated chips were used: one using pulsed immobilization, one incubated at 37 °C for 3 hours (no pulse), and one in which the DNA was added for 2 minutes and rinsed out immediately. A 20 ul aliquot of 160 nM DNA concentration was used in each case and all chips were rinsed three times with deionized water before measuring fluorescence intensity.
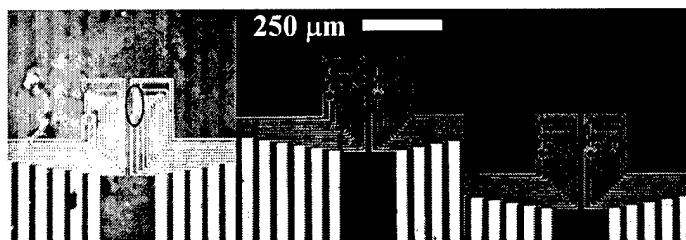

Figure 27: 160 nM DNA immobilized on three glass chips. Left to right: pulse-assisted immobilization, passive (incubated for 3 hrs. at 37 ℃) immobilization, and control chip exposed to DNA solution for 2 mins. and rinsed.

The relative fluorescent intensity was averaged for each chip in the portion circled in red. Intensity of the pulse-immobilized chip was 493 R.U., while the passive and 2 minute exposed chips were 286 and 243 R.U., respectively. There appeared to be splotches on the passive chip of areas that were brighter than their neighbors, suggesting the self-assembled monolayer may have not properly attached to the surface. Although the pulse was only applied between two electrodes within the circle, like the authors of [19, 20] we observed a fairly uniform coverage over the entire area of the chip covered with the DNA solution.

H. Modeling Kinetics of Solid Phase DNA Hybridization

Some preliminary development of a model for the kinetics of DNA hybridization using solid phase attachment chemistry was developed this quarter.

The solid surface with immobilized probe ssDNA was characterized as below:

1. $C_{s,max}$: possible maximum surface DNA concentration
2. C_p: immobilized probe ssDNA concentration
3. C_a: adsorbed ssDNA concentration
4. C_{ds}: hybridized dsDNA concentration

The following relationships hold true:

1. $C_p + C_a \leq C_{s,max}$
2. $C_{ds} \leq C_p$
3. $C_{b0} \leq C_{s,max}$ (C_{b0} is the effective bulk target ssDNA concentration for hybridization)

There are there concurrent "reactions" as showing in figure 28:

1. Hybridization of bulk target ssDNA and immobilized probe ssDNA with binding rate coefficient $k_1{}^1/k_1{}^{-1}$, $[C_{b0}]+[C_p-C_{ds}] \Leftrightarrow [C_{ds}]$
2. Adsorption / Desorption of bulk target DNA onto the surface with rate coefficient k_a/k_d, $[C_{b0}]+[C_{s,max}-C_p-C_a] \Leftrightarrow [C_a]$
3. Hybridization of adsorbed target ssDNA and immobilized probe ssDNA with binding rate coefficient $k_2{}^1/k_2{}^{-1}$, $[C_a]+[C_p-C_{ds}] \Leftrightarrow [C_{ds}]$

Then C_{ds} and C_a are governed by the following equations,

$$\frac{\partial C_{ds}}{\partial t} = \left[k_1{}^1 C_{b0}\left(C_p - C_{ds}\right) - k_1{}^{-1}C_{ds}\right] + \left[k_2{}^1 C_a\left(C_p - C_{ds}\right) - k_2{}^{-1}C_{ds}\right] \tag{11}$$

$$\frac{\partial C_a}{\partial t} = \left[D_a \nabla^2 C_a\right] + \left[k_a C_{b0}\left(C_{s,max} - C_p - C_a\right) - k_d C_a\right] - \left[k_2{}^1 C_a\left(C_p - C_{ds}\right) - k_2{}^{-1}C_{ds}\right] \tag{12}$$

In equation (12), the first term on the right hand is the diffusion of adsorbed target ssDNA on the solid surface.
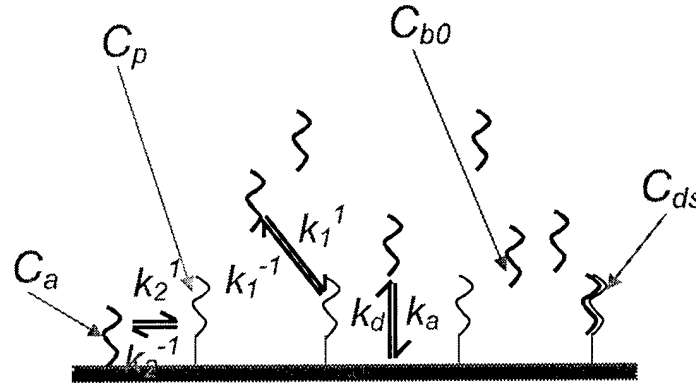

Figure 28: The hybridization of bulk target ssDNA to probe ssDNA immobilized on a solid surface. Three concurrent "reactions" are shown.

Neglecting the surface diffusion effects, equations (11) and (12) can be easily integrated. First, we check the effects of C_{b0}. When $k_2{}^1=k_1{}^1=k_a=0.1$, $k_2{}^{-1}=k_1{}^{-1}=k_d=0.001$, $C_{s,max}=2$, $C_p=1$, figure 29 depicts C_{ds} and C_a as functions of time (right: $C_{b0}=0.1 \times C_{s,max}$, left: $C_{b0}=C_{s,max}$). The time required to reach saturation is reduced about 8 times from $C_{b0}=0.1 \times C_{s,max}$ to $C_{b0}=C_{s,max}$. We define the hybridization time, $\tau_{0.9H}$, as the time required for hybridization to reach 0.9 times the level of saturation. Figure 5 depicts $\tau_{0.9H}$ as a function

of $\dfrac{C_{b0}}{C_{s,\max}}$. It is found that $\tau_{0.9H}$ is almost proportional to $C_{b0}^{-0.8}$. So, increasing C_{b0} will decrease hybridization time correspondingly.
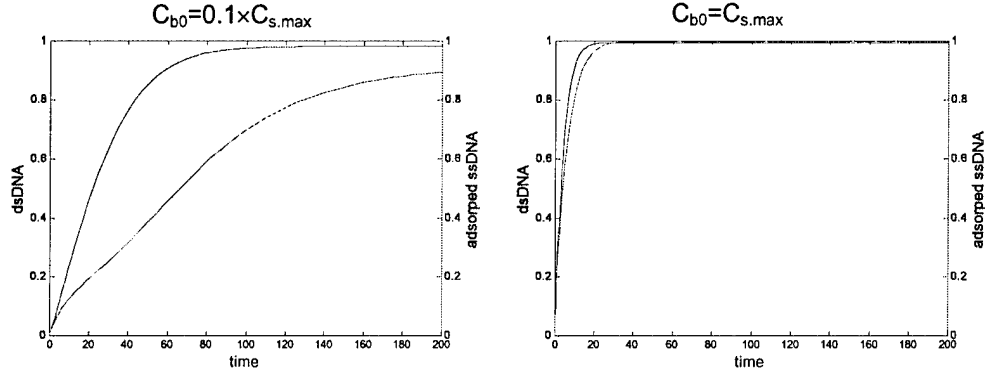

Figure 29: Concentrations of hybridized dsDNA and adsorbed ssDNA as a function of time when $k_2^{1}=k_1^{1}=k_a=0.1$, $k_2^{-1}=k_1^{-1}=k_d=0.001$, $C_{s,max}=2$, $C_p=1$.
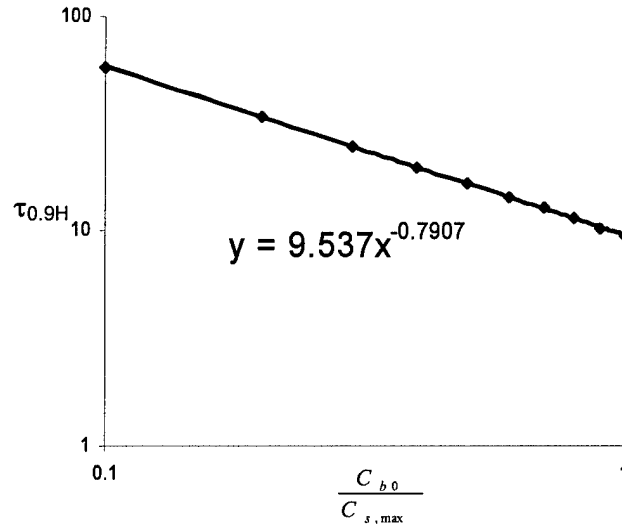

Figure 30: The hybridization time as a function of effective target ssDNA concentration when $k_2^{1}=k_1^{1}=k_a=0.1$, $k_2^{-1}=k_1^{-1}=k_d=0.001$, $C_{s,max}=2$, $C_p=1$.

We then study the effects of hybridization binding rate k_1^{1} on the hybridization time. Figure 6 depicts $\tau_{0.9H}$ as a function of k_1^{1} when $k_2^{1}=k_a=0.1$, $k_2^{-1}=k_1^{-1}=k_d=0.001$, $C_{s,max}=2$, $C_p=1$, and $C_{b0}=C_{s,max}$. The hybridization time decreases sharply as the binding rate increases, but the effects will saturate after the binding rate passes a certain value.
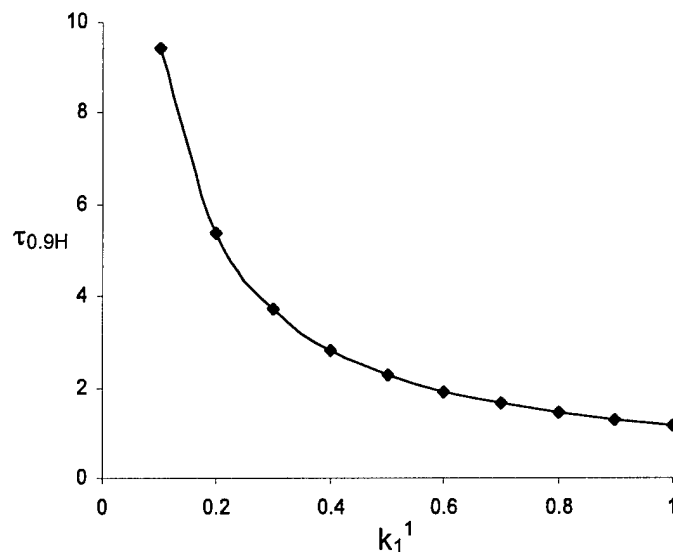
23

Figure 31: The hybridization time as a function of the binding rate when $k_2^{1}=k_a=0.1$, $k_2^{-1}=k_1^{-1}=k_d=0.001$, $C_{s,max}=2$, $C_p=1$, and $C_{b0}=C_{s,max}$.

I. Protein-small molecule (Streptavidin-biotin)

In order to determine if a protein-small molecule binding event is detectable in the nanogap, the interaction between biotin (Vitamin H) and the glycoprotein streptavidin (derived from *streptococcus avendii* bacterium) was studied. This interaction has one of the highest known affinity constants ($\sim$1015 M^{-1}) [and] is becoming popular as alternative to directly coupling markers to antibodies.

A summary of the protocol is as follows:

1. Silanize native SiO_2 surface using 3-aminopropyltriethoxysilane (chip now has terminal amine groups). Rinse well in EtOH and dry at 120 °C.
2. Add 30 ul deionized water and measure dielectric response of SAM-coated chip.
3. Incubate 40 mg/ml biotin in dimethyl formamide (DMF) on chip for 60 mins. at room temperature.
4. Rinse 3x in deionized water, add 30 ul deionized water, and measure dielectric response.
5. Incubate 0.2 mg/ml streptavidin dissolved in 0.15 M phosphate-buffered saline (PBS) for 20 mins. at room temperature.
6. Rpt. Step 3., but wash in successively lower concentrations of PBS until deionized water is reached. Measure dielectric properties in deionized water.

To check non-specific binding, we repeated the procedure using human serum albumin (HSA) as a control, instead of streptavidin. However, we were not able to easily discriminate changes from HSA from streptavidin, indicating some non-specific effects on the surface. In contrast to the changes observed with DNA, the permittivity appears to decrease slightly with each step. This can be explained by the

successive decrease of the effective gap size caused by selectively binding molecules to the surface, again leading to more overlap of the double layers.
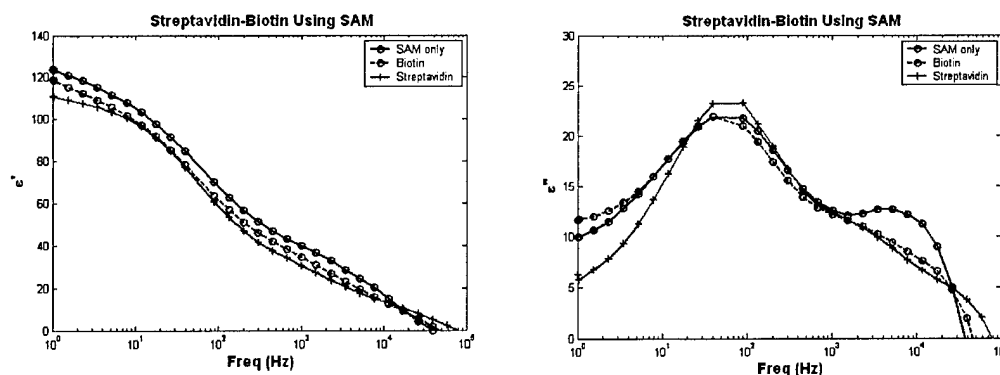

Figure 32: 1.2 ug biotin immobilized on the nanogap surface, followed by binding of 0.2 mg/ml streptavidin. All measurements are done in deionized water with the 'SAM only' one before the biotin.

J. Immunoassay: Ag-Ab (Laminin-Anti-laminin)

In order to show application to immunosensing, the nanogap was used to study binding between laminin, a glycoprotein clinically relevant to kidney disease, and its antibody. Though fairly high concentrations were utilized to insure the surface of the sensor was saturated in this proof-of-concept (0.1 mg/ml anti-laminin and 1 μg/ml laminin), the actually quantity needed is much smaller (2 ng of sample were in the 20 ul droplet, but less could be used in principle). The attachment chemistry is shown below.
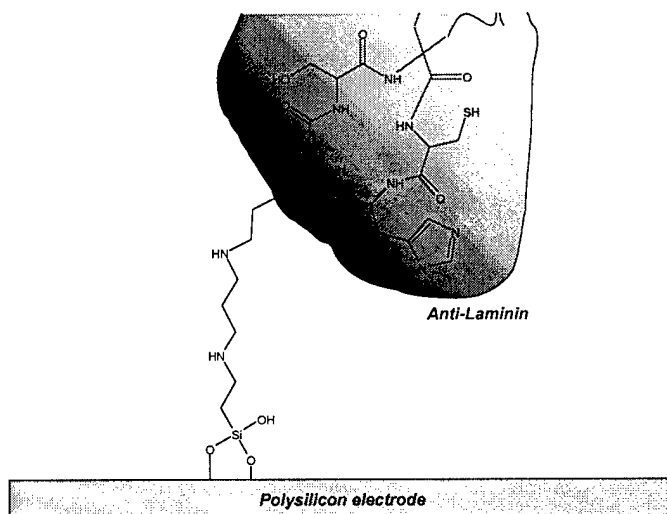
Figure 33: Glutaraldehyde forms an imine linkage with APTES. Anti-laminin is immobilized through attachment of primary amines (lysine residues at the N-terminus) to free aldehydes through more imine linkages. These were then reduced by addition of 10 mg/ml of sodium cyanoborohydride in 0.1x PBS. After washing to remove any unbound material, the devices were used for sensing experiments using the protein laminin or human serum albumin (HSA) for a control.

25

A summary of the protocol is as follows:

1. Use SAM protocol to functionalize surface with amines (Step 1. of protein-small molecule protocol)
2. React 2% glutaraldehyde in 0.1x PBS, pH = 7.4 (~15 mM NaCl) for 1 hr.
3. Incubate 0.1 mg/ml anti-laminin in 0.1x PBS, pH = 7.4 for 3 hr. at room temperature.
4. Complete Ab attachment with 15 mg/ml Na cyanoborohydride in 0.1x PBS, pH = 7.4 for 1 hr. at 4 °C.
5. Incubate protein (either laminin or HSA) at 1 ug/ml in 0.1x PBS, pH = 7.4 for 30 mins.

We measured the dielectric properties after each step above using the 4th aliquot of the 0.1x PBS wash buffer each time (used to remove excess, unreacted species at each step). This is a compromise between possible conformational changes (denaturation) at low salinity and reducing ion shielding effects for the dielectric measurement.
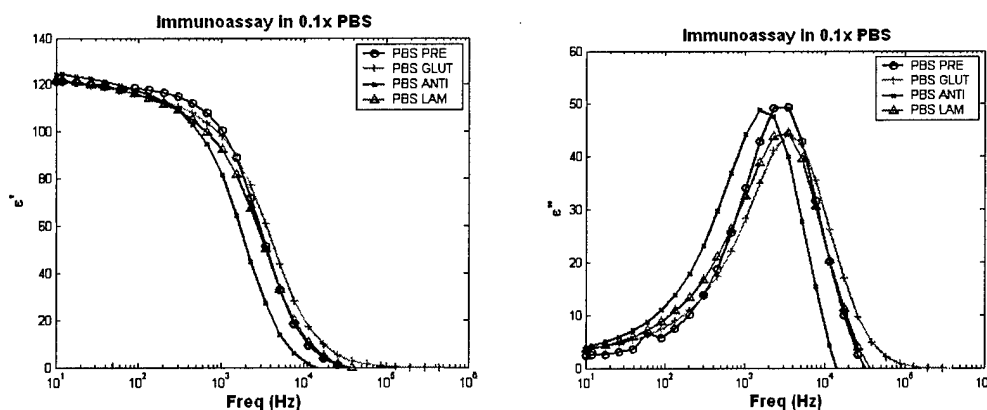
Key: Pre – SAM in PBS alone before glutaraldehyde (GLUT), anti-laminin (ANTI), laminin (LAM)

Figure 34: Dielectric spectra captured for sequential steps in the immunoassay.

Most replicates showed decreases in the imaginary part of the permittivity as the surfaces were modified with the proteins. In particularly, the antibody (anti-laminin) resulted in an increase in the real part of the permittivity at frequencies below 1 kHz and a corresponding frequency shift of the dispersion to lower frequencies. Perhaps half of the devices used for the experiments failed at this step, indicating possible clogging of the nanogap. This was accompanied by a monotonic increase in the imaginary permittivity (which corresponds to the device resistance) at low frequencies, suggesting the antibody spanned the gap. This could allow charge transfer and seemed to "short" the response. We were not able to show specificity for laminin in controls with human serum albumin (HSA), suggesting we may be sensitive to molecules non-covalently bound on the surfaces by, for example, van der Waals and other forces. Below is an example of this that occurred at the laminin step:
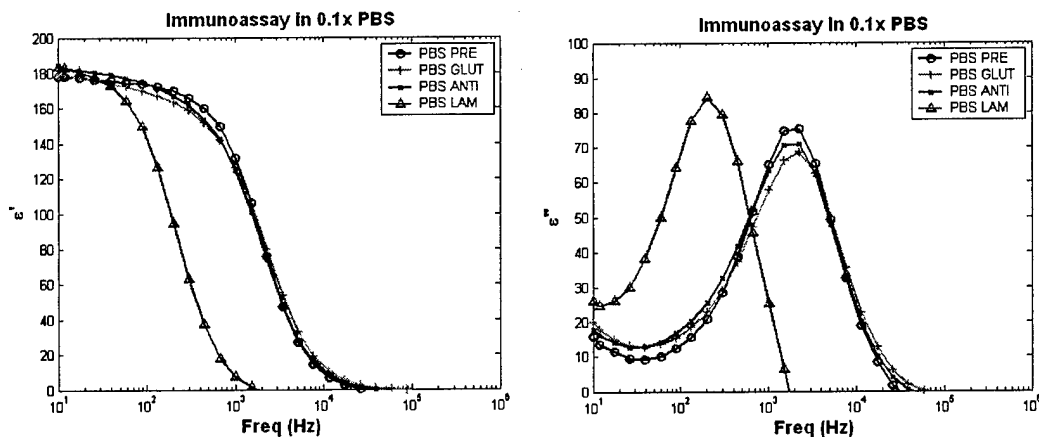
Figure 35: Dielectric spectra for immunoassay showing large change after laminin addition. Chips were washed three times each in 0.1x PBS (soaked for 1 min. per wash), which may not have been enough to remove residual material in the gap.

K. Variability Study – Effects of Sample Loading and Probe Contact

In using the nanogap with our wafer probe station and silicone "well" structure (Fig. 2), we noted several sources of error that required further study. Since we were simply concerned with variations, results of these investigations are shown in terms of the capacitance and loss tangent, rather than converting to real and imaginary permittivities.

Electrical calibration using a short, open, and load was performed to the end of the coaxial cable connected to the dielectric analyzer. From there, a second shielded cable was connected via a BNC connector to the micromanipulator, which in turn contacted the device. This second cable was shielded up to the point at which it was soldered to the manipulator brass arm. Thus, perhaps 6" of unshielded conductor was exposed, which consistently produced several small low frequency noise spikes around 60 and 300 Hz for dry samples. In repeatedly contacting the device, we observed a significant amount of variability (> ± 2.5%) even for dry measurements above 100 KHz:
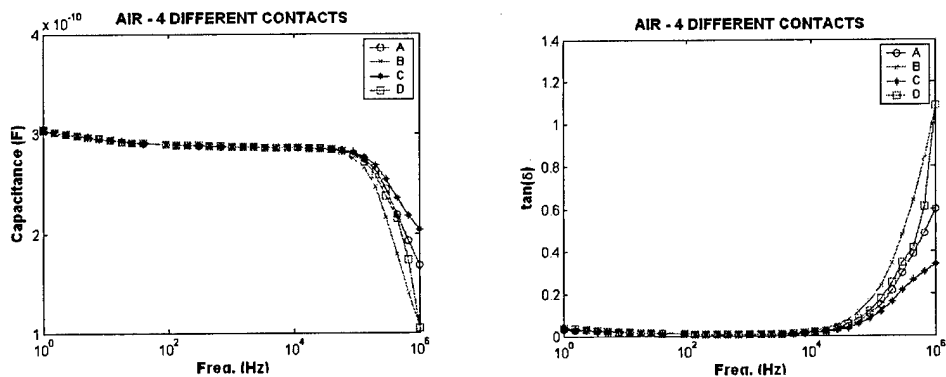

Figure 36: Dielectric properties of nanogap in air, repeatedly contact the surface at different locations.

These differences are likely caused by small changes in shape of the probe tips that influence the inductance. Since we do not calibrate to the end of the probe tip and the inductance scales as frequency ($Z_L = j\omega L$), this effect is more pronounced near the MHz regime. We repeated the measure for deionized water, contacting 10 times in different locations:
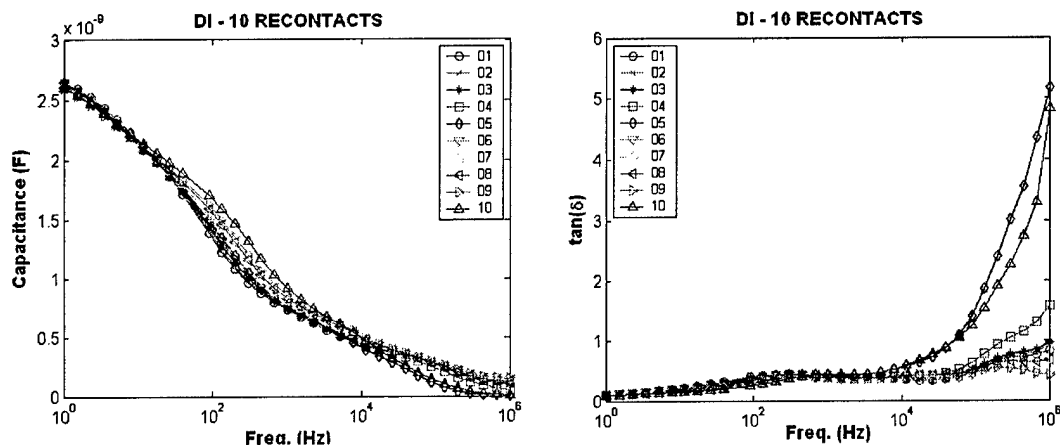

Figure 37: Dielectric properties of nanogap in water, repeatedly contact the surface at different locations.

Contacts '05' and '010' above yielded much high loss tangents, often more than double the expected value. Thus, we estimated perhaps 20% of the time incorrect contacts could result in false reads. The monotonic increase in frequency that was observed can be attributed to evaporation of the sample, since the same aliquot of DI was used for more than 40 mins. and no attempt was made to cover it.

We also tested the effects of loading a sample of deionized water into the nanogap multiple times. For these experiments we placed a 30 µl droplet of DI in the silicone well, measured the dielectric properties, removed the droplet by wicking using a clean strip of disposable cloth, and repeated several times (using the same DI solution).
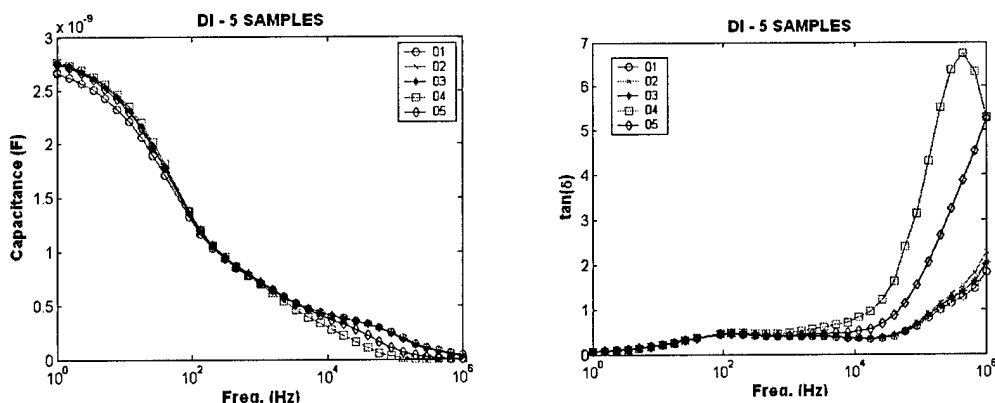

Figure 38: Dielectric properties of nanogap in water, repeatedly loading different samples into the same device.

There is significantly more variation in these five samples above 1 KHz. However, if we consider on the cluster of three (red, green, and blue) that are closer together, the error at 100 KHz is about ± 5%).

After learning about sample loading and contacting issues, we generally duplicated measurements with two independent loads or contacts where necessary and insured that the high frequency readings did not grossly deviate from one another in the course of using a given device.

L. Aqueous Filling of Nanochannels Using Optical Microscopy

Because of problems related to filling the nanogaps using a silicone well approach, we also tested sample loading by simply covering the device with a thin PDMS (silicone) membrane 150 μm thick for various channel widths and placing a droplet at the end of the device:
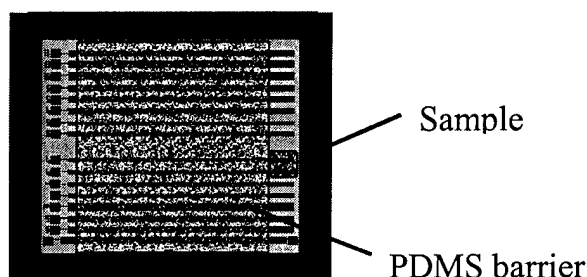
Figure 39: Nanogap chip with thin PDMS membrane showing sample droplet on surface. Channels fill by capillary force.
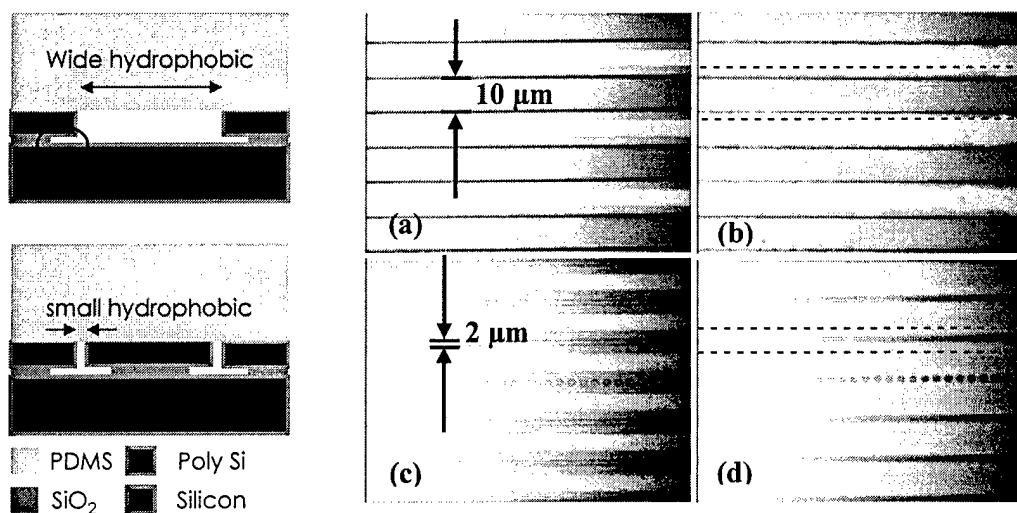
Figure 40: 300 nm deep nanogap channels filled with 2 nm gold nanoparticle solution (a) air in 10μm width (b) solution in channel (c) air in 2μm width (d) solution in channel. Gap area appears red, oxide is yellow (both viewed through poly-Si), bare silicon is blue in photos (a),(c). When liquid (deionized water) wets channels in (b),(d), they appear yellow. More uniform wetting is obtained for narrower widths (distance between adjacent gaps across the top of the device) because there is less hydrophobic interaction with the silicone (PDMS) cap.

29

Although sample loading using this approach was successful for native SiO_2 surfaces on the silicon devices, it was still difficult using DNA samples or surfaces coated with the hydrophobic self-assembled monolayer (3-aminopropyltriethoxysilane) used for immobilizing the DNA on the surface. Because of these problems in initial studies (see Fig. 41), we continued to use the well approach or just covered the entire surface of the chip with liquid samples. These issues will be addressed in the next quarter.
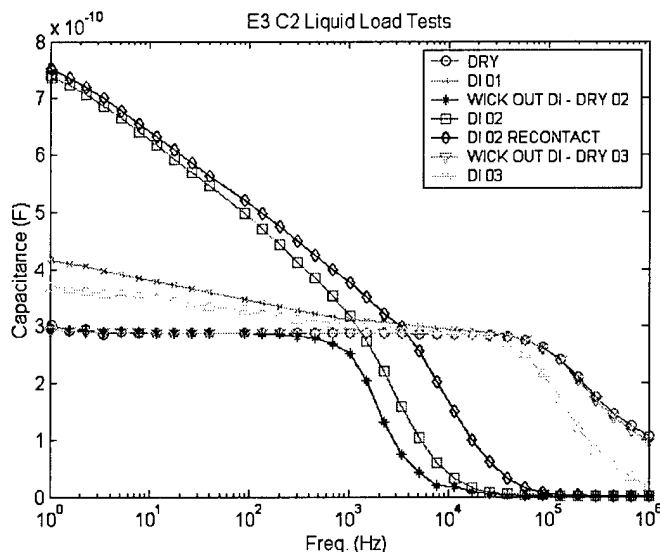

Figure 41: Deionized water loaded several times into nanogap with 2 μm width. Sample 02 loaded correctly (magenta and a contact remade in black), but 01 (green) and 03 (yellow) did not, appearing very much like air (red).

Issues with Current Sensor for Dielectric Relaxation Spectroscopy (DRS)

As can be seen by from the variability study in the last section, several issues will be addressed in the next quarter to improve reproducibility. Firstly, delivering the biological samples into the device in a consistent manner, free from entrained air pockets and such that the same area is wetted, has proven difficult with the current design. This is particularly observed with samples such as DNA and proteins, which tend to adhere to each other and to the device surfaces. Since the chemistry developed for covalent attachment to silicon oxide involves a hydrophobic self-assembled monolayer, consistent wetting of devices for experiments with surface-bound biomolecules was also difficult. In dielectric spectroscopy, most workers utilize a sample cell that is elastomerically sealed (using an O-ring or gasket) to limit evaporation of liquid samples. Although this usually means changing samples is more cumbersome, this avoids the issue of ionic concentration changes that accompany water loss and greatly influence measuring permittivity. Finally, particularly for experiments using surface-immobilized molecules, it is beneficial to be able to rinse unbound species by flushing the sample with buffer or deionized water. This is time consuming in an architecture without a closed chamber where liquid can only be exchanged using a pipette.

30

Secondly, temperature control and proper electrical connectivity are important dielectric spectroscopy. Typically, conductivity (σ or ε'') increases with temperature [9], so it is important to control or at least monitor temperature during data acquisition. As was also shown in the variability study, eliminating variations in contact impedance are critical for accurate measurement at frequencies over 10 kHz.

Lastly, as discussed in the introduction, the response of our current sensor is controlled by electrode polarization. This phenomenon is caused by the accumulation of free ions on electrode surfaces at low frequencies. It is apparent in the nanogap device by observing the power law dependence of the real permittivity (or capacitance) at low frequencies for our aqueous samples [23]. If the sample impedance itself was responsible, we should recover the permittivity of the solvent (water) at high frequencies and the permittivity should be roughly constant above 1 KHz (varying perhaps only 10-20%, but not strongly decaying). In other words, we should be able to discriminate the permittivity of the buffer itself from the biomolecules in the same to reveal frequency dispersions intrinsic to the sample. Many workers have proposed methods to deal with polarization, but most are cumbersome: 1) measure repeatedly at various electrode spacing (can then subtract polarization), 2) increase distance between electrode spacing (so that impedance of sample is large in serial model – see [23]), 3) substitute biological sample with similar solvent containing no sample (e.g., buffer), 4) coat electrodes with electroplated Pt black film, 5) measure at high frequency (>100 KHz) or partially correct with 3-terminal measurement [9], or 5) use a 4-probe scheme (using two electrodes to measure away from double layer).

In order to partially address these issues, we are purchasing a standard Novocontrol dielectric cell designed for high conductivity liquids. In conjunction with temperature control and a metal housing for shielding stray electric fields, this approach will limit errors from repeated electrical contacts, since the coaxial cables are hard wired to the gold-plated electrodes defining the cell.

Since the measurement volume of the Novocontrol dielectric cell is roughly 500 μl, there is benefit to considering miniaturizing the cell in the future. In order to study biomolecules in solution, a design that minimizes electrode polarization effects but allows easy liquid filling and flushing of the device, temperature control, and good electrical contact is being considered. An early concept of such a device is shown below:

Fluidic port

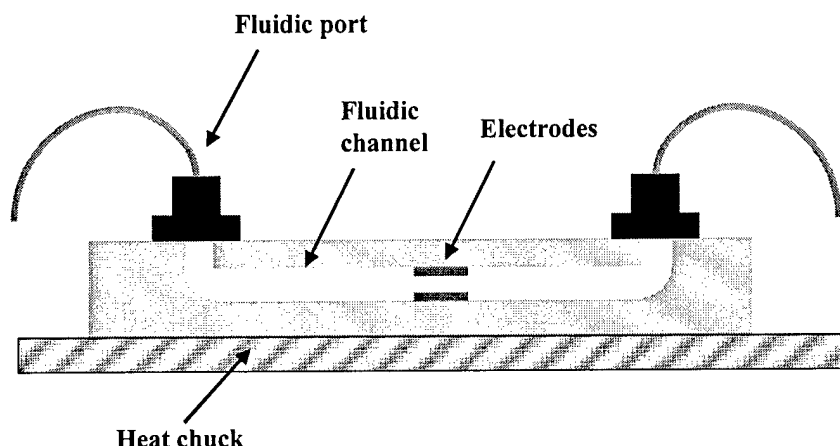**Fluidic channel**

Electrodes

Heat chuck

Figure 42: Concept for a microfabricated dielectric cell. Fluidic ports and a flow-through channel allow easy flushing and sample loading (particularly if small quantities of surfactants can be used); while a heating chuck allows temperature control. Alternatively, the whole chip could be placed inside a thermal enclosure. To minimize polarization, electrode diameter could be roughly the size of the channel height (for example, 200 μm) without requiring more than 10-20 μl of sample. Wire bonding using a conventional semiconductor back-end step such as a dual in-line package (DIP) allows a more robust electrical connection scheme.

Alternate Detection Schemes

Dielectric Relaxation Spectroscopy (DRS) is one of useful tool for characterizing the behavior of materials through charge redistribution in response to an externally applied electrical field. Typically, frequency domain dielectric relaxations termed "dispersions" are measured in liquid samples in a dielectric cell that, because of the design requirements outlined above, is not easily amenable to miniaturization or speed – prime requisites for a biological assay. If we are interested in studying biomolecular interactions, an approach that takes full advantage of a solid phase assay, in which the analytes are attached to a surface, is advantageous for several reasons. Firstly, low concentrations of samples can be utilized, since the molecules will self-concentrate on the surface (until saturation). Secondly, using DRS instrumentation with a device that is sensitive to polarization (such as the nanogap) is best utilized by immobilizing molecules on surfaces, since measuring in solution has proven insensitive. Finally, devices consisting of arrays of devices such as DNA and protein microarrays have flourished using a solid phase format.

To study biomolecular interactions at surfaces, there are a variety of techniques that are useful in detecting binding events. In particular, past work has been done using electrochemical impedimetric techniques such as cyclic voltammetry (CV) for measuring biological and chemical reactions on surfaces [15-18, 21]. Little work, however, has been reported using poly silicon electrodes with silicon dioxide passivation. In a basic electrochemical three-cell configuration, a potential is applied between the working and counter electrodes that allows current to pass through them. A separate, non-polarizable reference electrode and voltmeter with high input impedance is used to accurately monitor the potential at the working electrode, drawing very little current through the reference.
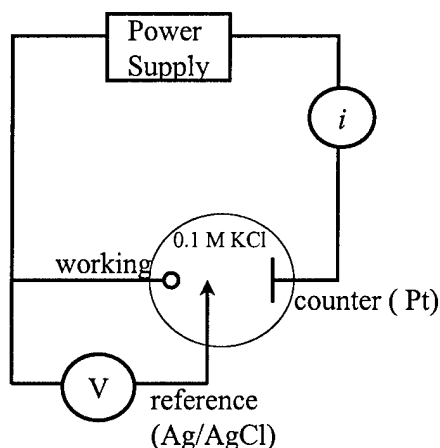
32

Figure 43: Typical three electrode configuration showing non-polarizable reference, counter, and working electrodes with a typical electrolyte.

Such as set-up could also be used with a potentiostat to study the surface coverage densities of self-assembled monolayer and biomolecules on the surface of the nanogap to further validate the attachment chemistries. Once coverage is better understood, SAMs of various lengths and end groups with different charges could be used to explore modulation of the double layer in the nanogap using either dielectric spectroscopy or an electrochemical technique.

An alternate concept to realizing the nanogap might be to create electrically addressable areas or spots on one wafer alternating with areas containing a 10-100 nm thick spacer. A second wafer could be used to make electrical contact and encapsulate the structure using a positioning jig. In this way, other techniques like surface plasmon resonance (SPR), atomic force microscopy (AFM), or total internal reflection (TIR) microscopy could be used to validate and/or optimize biological protocols as a prelude to electrical detection. Depending on proof-of-concept work, one of these techniques may prove more amenable to studying biomolecular interactions and still afford the advantages of miniaturization by reducing sample consumption and increasing throughput.
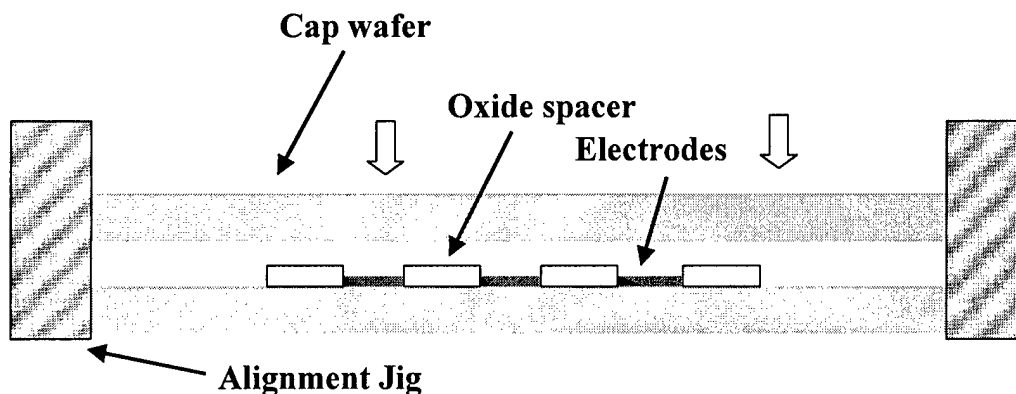

Figure 44: Alternate nanogap concept showing gold electrodes onto which biomolecules could be selectively attached via surface chemistry. Wafers could be assembled using an alignment jig and clamping in buffer solution.

33

4. System Testing and Biological Assay

Regardless of the detection scheme employed, work next quarter will involve system level tests designed to quantify major "noise" sources and accurately assess reproducibility. Temperature, sample loading, and electrical contact, for example, affect dielectric measurements and need to be addressed. Once these concerns are mitigated, an example of a simple biological assay would be to test different concentrations of single-stranded DNA either in solution or immobilized to a self-assembled monolayer and demonstrate the result is significantly different from the buffer in which it is measured (or the native SAM-coated surface).

5. Summary

A dielectric spectroscopy (DS) using nanogap electrode to measure small molecules in solution was demonstrated for various gap sizes. Permittivity measurements were strongly influenced by electrode polarization, which manifested itself across the entire frequency spectrum due to the high ratio of device area to distance between the electrodes. This was investigated by testing DNA solutions in several buffer concentrations. It was confirmed that ionic strength differences in the buffers were responsible for the changes in permittivity. A simple lumped element model for the devices in air was constructed. Attachment chemistry for immobilizing biomolecules using primary amines via a self-assembled monolayer was validated and later utilized.

DNA hybridization using passive (incubation at 3 hours, 42 °C) and ultrafast electric-field pulse enhancement methods was carried out and confirmed using fluorescence and dielectric spectroscopy. A model of DNA hybridization kinetics was constructed that will allow determination of rate constants with further experiments in the next quarter if funding is provided. Preliminary work using the nanogap for a protein-small molecule assay (steptavidin-biotin) was also performed that showed a decrease in permittivity as subsequent molecules were assembled on the surface. This agrees with previous work using electrochemical detection methods. An immunoassay using a clinically relevant glycoprotein (laminin) was repeated.

Recently, label-free detection of conformational changes of ferricytochrome c (cyt-c) molecules in aqueous solution was achieved using a unique nanocavity device that enables low frequency DS. Low frequency DS is typically avoided as a method for material characterization because the signal is dominated by electrode polarization and solution conductivity effects. Using a nanogap sensor, we present data indicating that these effects are reduced when compared with a commercially available dielectric cell. This result demonstrates that this nanogap sensor can presents a powerful potential platform for identifying the conformational states of proteins. In addition, these devices can be easily fabricated into formats that are amenable to high density benchtop proteomic systems.

6. PUBLICATIONS & PRESENTATIONS

1. M. Yi, K. Jeong, and L. P. Lee, '"Theoretical and Experimental Study towards a Nanogap Dielectric Biosensor," *Biosensor and Bioelectronics* (accepted 2004).

2. Dino Di Carlo, Joshua. T. Nevill, Peng Liu, Ki-Hun Jeong, and Luke P. Lee, "Low frequency dielectric spectroscopy using a nanogap sensor to detect conformational changes of ferricytochrome c in aqueous solution," *Biophysical Journal* (submitted).

3. M. Yi, L. Sison, K. Jeong, and L. P. Lee, "Effects of Electrical Double Layer Interaction within Nanogap Electrodes," *Journal of Colloid and Interface Science* (submitted).

4. H. Kang, J. Seo, D. Di Carlo, Y. Choi, and L. P. Lee, "Planar Nanogap Capacitor Arrays on Quartz for Optical and Dielectric Bioassays," *Proceedings of Micro Total Analsysis Systems 2003*, pp. 697-700, Squaw Valley, CA, USA, October 5-9, 2003.

5. S. Oh, J.S. Lee, K. Jeong, and L. P. Lee, "Minimization of Electrode Polarization Effect by Nanogap Electrodes for biosensor Applications," *IEEE MEMS 2003*, pp. 52-55; Kyoto, Japan, Jan. 19-23, 2003.

6. D. Di Carlo, H. Kang; X. Zeng, K. Jeong, and L. P. Lee, "Nanogap-based Dielectric Immunosensing," *TRANSDUCERS 2003, Solid-State Sensors, Actuators and Microsystems*, pp. 1180 – 1183, 2003.

7. J. Lee, Y. Choi, M. Pio, J. Seo and L. P. Lee, "Nanogap Capacitors for Label Free DNA Analysis," *Proceedings of Materials Research Society 2002 Spring Meeting*, pp. 185-190, April 1-5, San Francisco, CA.

8. **(Invited Paper)** L. P. Lee, "BioPOEMS & Nanogap DNA Junctions," *Proceedings of Micro Total Analsysis Systems 2002*, pp. 341-343, Nara, Japan, November 3-7, 2002.

9. J. Lee, S. Oh, Y. Choi, and L. P. Lee, "Label Free Dielectric Detection of DNA Hybridization with Nanogap Junctions," *Proceedings of Micro Total Analsysis Systems 2002*, pp. 305-307, Nara, Japan, November 3-7, 2002.

10. Y. Choi, J. Lee, and L. P. Lee, "Nanofabrication Technology of Nanogap Electrodes for Label Free DNA Chip," *Appl. Phys. Lett.* (submitted).

11. **(Plenary Speaker)** "BioPOEMS & Nanogap DNA Junctions," *International Conference on Micro Total Analsysis Systems*, Nara, Japan, November 3-7, 2002.

12. **(Plenary Speaker)** Biophotonic MEMS and Nanogap Bioelectronics," *The International Symposium on Microchemistry and Microsystems (ISMM 2002)*, Kanagawa, Japan, November 1, 2002.